

GUIDELINES

Diffusion-weighted MR spectroscopy: Consensus, recommendations, and resources from acquisition to modeling

Clémence Ligneul¹   | Chloé Najac²  | André Döring^{3,4}  | Christian Beaulieu⁵  |
 Francesca Branzoli⁶  | William T. Clarke¹  | Cristina Cudalbu^{4,7}  |
 Guglielmo Genovese⁸  | Saad Jbabdi¹  | Ileana Jelescu^{9,10}  |
 Dimitrios Karampinos¹¹  | Roland Kreis^{12,13}  | Henrik Lundell^{14,15}  |
 Małgorzata Marjańska⁸  | Harald E. Möller¹⁶  | Jessie Mosso^{4,7,17}  | Eloïse Mougel¹⁸ |
 Stefan Posse^{19,20}  | Stefan Ruschke¹¹  | Kadir Simsek^{3,21}  |
 Filip Szczepankiewicz²²  | Assaf Tal²³  | Chantal Tax^{24,25}  | Georg Oeltzschner^{26,27}  |
 Marco Palombo^{3,21}  | Itamar Ronen²⁸  | Julien Valette¹⁸ 

Correspondence

Clémence Ligneul, Wellcome Centre for Integrative Neuroimaging, FMRIB, Nuffield Department of Clinical Neurosciences, University of Oxford, Oxford, UK.

Email: clemence.ligneul@ndcn.ox.ac.uk

Funding information

Lorentz Center (Leiden, Netherlands), Grant/Award Number: ANR-11-INBS-0011

Abstract

Brain cell structure and function reflect neurodevelopment, plasticity, and aging; and changes can help flag pathological processes such as neurodegeneration and neuroinflammation. Accurate and quantitative methods to noninvasively disentangle cellular structural features are needed and are a substantial focus of brain research. Diffusion-weighted MRS (dMRS) gives access to diffusion properties of endogenous intracellular brain metabolites that are preferentially located inside specific brain cell populations. Despite its great potential, dMRS remains

Abbreviations: (B)PFG, (Bipolar) Pulsed field gradients; b-value, Diffusion-weighting (unit: $\text{ms}/\mu\text{m}^2$); b_0 , Minimum b-value required for spoiling; B_0 , Magnetic field strength; b_{max} , Maximum b-value used in an experiment; CNS, Central nervous system; CV, Coefficient of variation; Cr, Creatine; CSF, Cerebrospinal fluid; DDE, Double diffusion encoding; DTI, Diffusion tensor imaging; dMRI, Diffusion-weighted MRI; dMRS, Diffusion-weighted magnetic resonance spectroscopy; D_{intra} , diffusivity inside the cylinders or sticks; ECC, Eddy currents correction; EC, Eddy currents; FLAIR, Fluid-attenuated inversion recovery; FA, Fractional anisotropy; Glu, Glutamate; GM, Grey matter; GPC, Glycerophosphocholine; Ins, Myo-inositol; Kapp, Apparent kurtosis; MM, Macromolecules; NAAG, N-acetyl-aspartyl-glutamate; OG, Oscillation gradients; PCho, Phosphorylcholine; PCr, Phosphocreatine; PGSE, Pulsed-gradient spin echo; R , radius of the cylindrical structures comprising the randomly oriented infinite cylinders model; STE, Stimulated echo; SE, Spin echo; SGP, Short gradient pulse; SNR, Signal-to-noise ratio; SVD, Singular value decomposition; sLASER, semi-LASER, LASER=Localization by adiabatic selective refocusing; TM, Mixing time; Tau, Taurine; t_d , Diffusion time; tCho, Choline compounds; tCr, total Creatine; tNAA, total N-acetylaspartate; VOI, Voxel of Interest; WM, White matter; σ , std of the Gaussian noise underpinning the normalized dMRS signal decay; μFA , Microscopic fractional anisotropy.

Clémence Ligneul and Chloé Najac contributed equally to this work.

For affiliations refer to page 21

This is an open access article under the terms of the [Creative Commons Attribution-NonCommercial-NoDerivs](https://creativecommons.org/licenses/by-nc-nd/4.0/) License, which permits use and distribution in any medium, provided the original work is properly cited, the use is non-commercial and no modifications or adaptations are made.

© 2023 The Authors. *Magnetic Resonance in Medicine* published by Wiley Periodicals LLC on behalf of International Society for Magnetic Resonance in Medicine.

a challenging technique on all levels: from the data acquisition to the analysis, quantification, modeling, and interpretation of results. These challenges were the motivation behind the organization of the Lorentz Center workshop on “Best Practices & Tools for Diffusion MR Spectroscopy” held in Leiden, the Netherlands, in September 2021. During the workshop, the dMRS community established a set of recommendations to execute robust dMRS studies. This paper provides a description of the steps needed for acquiring, processing, fitting, and modeling dMRS data, and provides links to useful resources.

KEYWORDS

acquisition, dMRS, fitting, modelling, processing

1 | INTRODUCTION

The discovery that MRI can probe the diffusion process, and that the water in biological tissue was a ready-made, endogenous probe of tissue microstructure, ushered in an exciting era of innovation and development in diffusion-weighted MRI (dMRI). dMRI has numerous applications in neuroscience and clinical research. It also has several applications in clinical routine, including detecting stroke¹ and diagnosing prostate cancer.² With standard clinical MRI scanners, dMRI achieves spatial resolution on the order of millimeters, thanks to the abundance of water in tissue, although by mapping diffusion measures dMRI can reveal tissue structure on a microscopic length scale (microstructure). However, a challenge is the ubiquity of water in tissue and the heterogeneous nature of tissue microstructure, which leads to ambiguity in the interpretation of dMRI measurements. Almost concurrently with dMRI, diffusion-weighted MRS (dMRS) was developed to exploit the compartmental specificity of MR-detectable molecules other than water for diffusion-based microstructural investigations.

Early metabolite-focused investigations used phospho-metabolites by implementing phosphorus dMRS in the brain and muscle.^{3,4} Subsequently, proton (¹H)-dMRS measurements were made using endogenous molecules with discernible ¹H resonances, which are thus detectable and quantifiable with ¹H-MRS techniques. In the brain, for example, there are more than 10 detectable metabolites in the mM concentration range (Figure 1A). Most of them are predominantly intracellular and therefore provide a probe of intracellular cytomorphology. Some metabolites have nonuniform distributions across cell types. For example, the makeup of metabolites is different for neurons and astrocytes. Therefore, the relative concentrations of metabolites can be used to distinguish different cell types. Although the exact distributions of metabolites

across cell types is unknown, it is generally accepted that myo-inositol (Ins) and choline compounds (tCho = glycerophosphocholine, GPC + phosphocholine, PCho) are preferentially found inside astrocytes and glutamate (Glu) and NAA in neurons^{5–7} (Figure 1). Initially, measurements were done *in vitro*,⁸ and later *in vivo* in animal models^{9,10} and in humans.¹¹ These early dMRS studies delivered microstructural information on healthy and diseased tissue, otherwise unattainable with dMRI.¹² Subsequent and significant advances in MR hardware, acquisition techniques, modeling strategies, and computational abilities have allowed dMRS studies to provide unique insights on cellular morphology and physiology in health and disease. The history is eloquently summarized in several published reviews.^{13–17} In parallel, a better understanding of the factors that affect measurement accuracy in *in vivo* dMRS experiments led to more robust and reproducible measurements of diffusion metrics. This enabled meaningful dMRS studies in clinical populations and in animal models (see Figure 2). The result is a steady increase in the number and variety of dMRS studies across the MR community, also covering applications in tissues beyond the central nervous system (CNS) (c.f. box 1).

BOX 1 dMRS outside the brain

Although most dMRS applications are focused on the CNS, methods have also been developed in the body for various applications¹⁸:

- To measure water diffusion properties, which are not confounded by fat.^{19,20}
- To measure fat properties within adipose tissue.²¹ Best acquisitions schemes are described in Refs. 22–24. Specific vibration-compensation

schemes that might be required are described in Ref. 25.

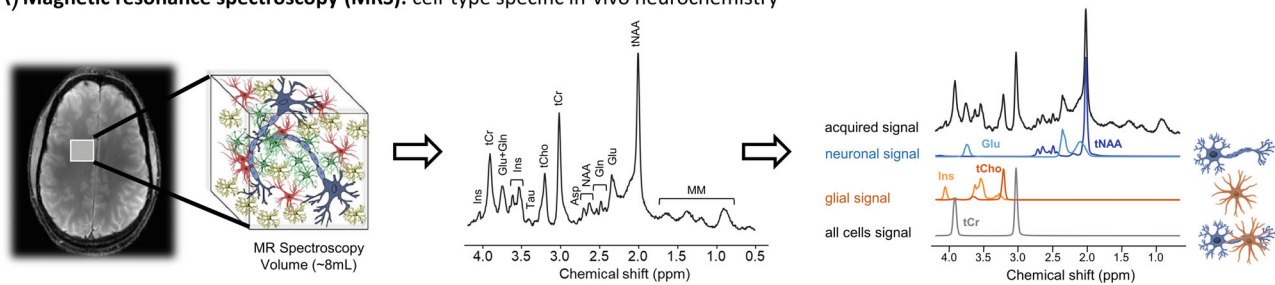
- To measure diffusion of lipid molecules such as intra- and extramyocellular lipids and less abundant metabolites within skeletal muscle.^{26,27} The optimal acquisition parameters for dMRS in body applications will depend on the size of the target molecule. In addition, the proper quantification of the diffusion properties of large molecules is challenging due to the confounding effect of physiological motion on the diffusion measurement.
- To separate overlapping peaks such as lactate and lipids.^{28–30}

Despite the great promise of a specific, noninvasive tool for measuring in vivo cytomorphology, the use of dMRS

in preclinical and clinical investigations remains limited. Most dMRS studies are performed by a small number of sites that are involved in developing dMRS methodology, or by groups in direct collaboration with experts from these sites. These interesting studies are typically small, proof-of-concept studies that show the potential of dMRS. However, the sparse adoption of dMRS indicates that methods are not yet simple and robust enough to garner traction from independent and nonexpert users.

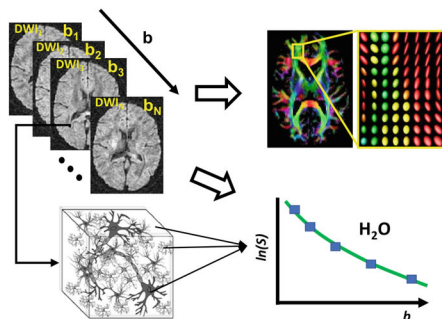
There are several challenges for a widespread adoption of dMRS. Foremost is the absence of robust, vendor-provided dMRS pulse sequences on commercial (human and animal) scanners; and second is a similar absence of readily available pipelines for processing and analyzing dMRS data. In addition, three other challenges may deter researchers from engaging in dMRS studies: First, is the perception among researchers and clinicians that dMRS studies are complex and difficult to perform. Second, dMRS results are inconsistent across sites, originating from sensitivity to differences

(A) Magnetic resonance spectroscopy (MRS): cell-type specific in-vivo neurochemistry



(B) Diffusion-weighted imaging (dMRI): microstructure at

- **high spatial resolution,**
- **low compartmental and cell-type specificity**



(C) Diffusion-weighted MRS (dMRS): microstructure at

- **low spatial resolution,**
- **high compartmental and cell type specificity**

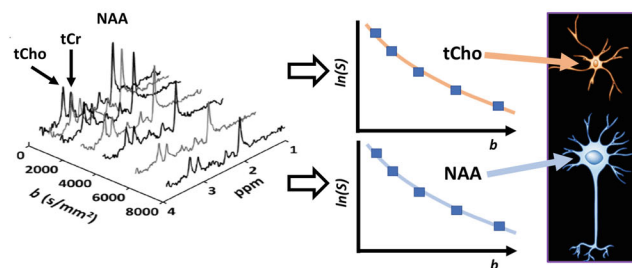


FIGURE 1 (A) MRS is the only neuroimaging tool providing in vivo noninvasive information on concentration of intracellular neuronal and glial metabolites. Whereas total NAA (tNAA = NAA + NAAG) and Glu are found primarily in neurons, choline compounds (tCho = PCho+GPC) and *myo*-inositol (Ins) are mainly located in glial cells. Other metabolites, such as total creatine (tCr = Cr + PCr) are found in all cells. (Figure adapted from Palombo et al.¹⁴) (B) dMRI probes neural tissue microstructure via sensitization to the diffusion of water in tissue. Analysis of dMRI data provides microstructural information at high spatial resolution but with no compartmental specificity because water is distributed across cells and tissue compartments. (C) dMRS is based on sensitization of MRS to diffusion in a similar manner to dMRI. The diffusion properties of neuronal (e.g., NAA) and glial (e.g., tCho) metabolites reflect the specific microstructural environment of their host cell type. dMRI, diffusion-weighted imaging; dMRS, diffusion-weighted MRS; tCho, choline compounds; PCho, phosphorylcholine; GPC, glycerophosphocholine; Glu, glutamate; NAAG, N-acetylaspartate glutamate; tCr, total creatine; Cr, creatine, PCr, phosphocreatine.

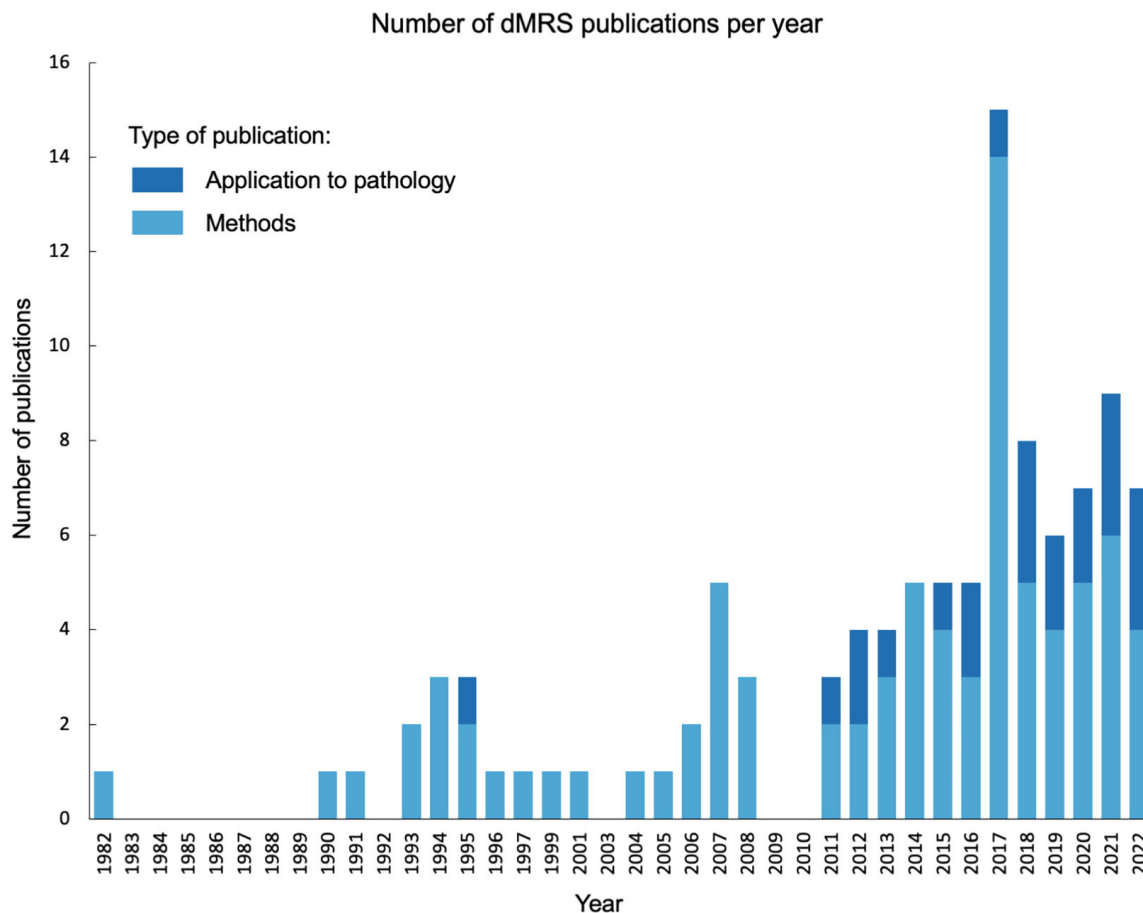


FIGURE 2 Number of dMRS publications per year. The dark blue tip corresponds to publications where dMRS is used to explore a brain disease (human) or a model of brain disease (animal). These publications were identified with a PubMed search initially yielding 196 results, curated to 114 results. Search criteria were: “diffusion weighted magnetic resonance spectroscopy” OR “dw-mrs” OR “diffusion-weighted mrs” OR “diffusion mrs” OR “diffusion weighted MR spectroscopy” OR “metabolites diffusion” OR “diffusion weighted NMR spectroscopy” OR “diffusion MR spectroscopy” OR “diffusion NMR spectroscopy” OR “diffusion magnetic resonance spectroscopy” OR “diffusion tensor spectroscopy”. All chemistry papers (typically identifying protein structures) were manually removed. Yoshizaki et al., *Biophys J*, 1982; Van Zijl et al., *PNAS*, 1991; Merboldt et al., *MRM*, 1993; Van Gelderen et al., *J. Mag. Res.*, 1994; Wick et al., *Stroke*, 1995; Pfeuffer et al., *NMR Biomed*, 1998; Pfeuffer et al., *JCBFM*, 2000; Shemesh et al., *Nature Comm*, 2014; Branzoli et al., *NMR Biomed*, 2014; Lundell et al., *NeuroImage*, 2021 were manually added. These papers are referenced on the MRShub dMRS forum (<https://forum.mrshub.org/t/educational-getting-started/946/3>).

in acquisition, processing, and analysis methods. This gives the impression that dMRS is not reliable enough, for example, to provide biomarkers of disease. Finally, the long acquisition time of dMRS experiments suggests that dMRS is incompatible with investigations in clinical populations.

These challenges were the motivation behind the organization of the Lorentz Center workshop on “Best Practices & Tools for Diffusion MR Spectroscopy” (<https://www.lorentzcenter.nl/best-practices-en-tools-for-diffusion-mr-spectroscopy.html>) held in Leiden, the Netherlands, in September 2021. The community of dMRS developers, together with that of MRS quantification experts, has established a set of common goals to make all components of the dMRS pipeline, from acquisition via

processing and analysis to modeling, readily available and openly accessible.

This paper provides step-by-step recommendations that were identified during the workshop for planning and executing a robust dMRS study. Throughout this paper, we will assume that the reader has knowledge of basic MRS concepts and is interested in incorporating dMRS in their research protocols. The focus is on the brain, but most recommendations from sections 2–4 hold for non-CNS applications (c.f. box 1). In the first section, we provide an overview of dMRS pulse sequences used for data acquisition, and we clarify under which conditions each should be used. We provide guidelines for choosing diffusion-weighting schemes and optimal diffusion-weighting parameters, depending on the desired

outcome of the experiment. In the second section, we lay out the processing steps that are required to maximize data quality by minimizing controllable inaccuracy and uncertainty affecting dMRS metrics. The third section is dedicated to practices related to spectral fitting of dMRS data for optimal retrieval of dMRS metrics such as metabolite ADC. The fourth and final section discusses key aspects of the dMRS signal in relation to brain microstructure and proposes the randomly oriented infinite cylinders model as an acceptable minimal biophysical model, within a given applicability framework. Finally, some examples of future directions for dMRS are listed.

2 | DMRS ACQUISITIONS

In this section, we will cover the acquisition of dMRS data, spanning from the choice of the sequence to the experimental setup itself.

2.1 | Choosing the right pulse sequence

The choice of the dMRS sequence is governed by the research question (e.g., what parameters are of interest) and the locally available sequences and hardware (e.g., what are the limitations). dMRS beginners can find contacts for available sequences on the dMRS section on MRShub (<https://forum.mrshub.org/t/sequences-and-acquisitions-strategies-for-dw-mrs/934>).

2.1.1 | STE versus SE

There are two broad categories of DW-sequences: those based on a stimulated echo (STE), in which the diffusion-weighting gradient moment builds up during the mixing time (TM) (being essentially the diffusion time [t_d]); and those based on a spin echo (SE), in which

diffusion-weighting gradient moment builds up entirely within the TE.

The advantage of STE-based sequences is that very large b -values can be achieved while maintaining short TE. In addition, STE-based sequences enable long t_d (particularly important when probing slowly diffusing metabolites and large diffusion restriction barriers). However, half of the signal is lost when using STE. The advantage of SE is essentially that it retains full signal. However, in practice, reaching long t_d or very large b -values requires long TE, which will in turn result in significant signal loss due to T_2 relaxation (and due to J -modulation for metabolites such as Glu or Ins).

Recommendations about the choice of sequence are summarized in Table 1. Sequence parameters (TE, TR) need to be carefully chosen depending on field-specific relaxation parameters.³¹ Animal and human scanners have different hardware capabilities; hence, different pulse sequences are presented here.

2.1.2 | Pulse sequences for human scanners

STE-based diffusion measurements on human scanners are preferably performed using STEAM^{11,32} (Figure 3A). Because long TM enables high b -values while keeping diffusion-weighting gradient strengths relatively low, for example, not larger than spoiler or slice-selection gradients, cross terms might be significant and must be taken into account (see box 2).

BOX 2 Cross terms

Diffusion gradients are the main contributor, but other gradients in the sequence also contribute to the diffusion weighting. As described in Ref. 36, the calculation of the b -value follows:

TABLE 1 Overview of recommended sequences for human and animal scanners, depending on the research question

Interested in	Stimulated echo or spin echo?	Human scanner	Animal scanner
Mostly singlets (tNAA, tCho, tCr)	Spin echo	BPGF-sLASER	SE-LASER
J -coupled metabolites (Glu, Ins, Tau)	Stimulated echo	PFG-STEAM	STE-LASER
Very high b -values	Stimulated echo	PFG-STEAM	STE-LASER
Long diffusion times	Stimulated echo	PFG-STEAM	STE-LASER
Advanced encoding: OG, DDE	Spin echo	OG/DDE-sLASER	OG/DDE-LASER

Abbreviations: (B)PFG, (bipolar) pulsed field gradients; DDE, double diffusion encoding; Glu, glutamate; Ins, *myo*-inositol; LASER, localization by adiabatic selective refocusing; OG, oscillating gradients; SE, spin echo; STE, stimulated echo; Tau, taurine; tNAA, *N*-acetylaspartate + *N*-acetylaspartylglutamate; tCr, Cr + phosphocreatine; tCho, phosphocholine + glycerophosphocholine.

$$b = -\gamma^2 \int_0^{T_{\text{seq}}} \left[\int_0^{t''} (G_{\text{diff}}(t') + G_{\text{others}}(t')) dt' \right]^2 dt''.$$

when G_{diff} (diffusion gradients) and G_{others} (other gradients, typically localisation gradients and/or spoilers) are intertwined, like in the STEAM-based and sLASER-based dMRS sequences, a cross term $\int G_{\text{diff}} \int G_{\text{others}}$ appears. To estimate the true b -value, this term must be calculated and taken into account because it grows with the diffusion gradient strength (unlike $\int G_{\text{others}} \int G_{\text{others}}$, which is a constant contribution at all b -values).

The calculation of the true b -value can be incorporated directly into the sequence code or calculated a posteriori based on the sequence chronogram. Examples of codes are openly available on MRS hub (<https://forum.mrshub.org/t/processing-for-dw-mrs/935>) to numerically compute the b -value based on the chronogram. It is possible to check in a phantom whether cross terms should be accounted for. Note that standard MRS sequences are slightly diffusion-weighted. The residual b -value with no diffusion gradient depends on the hardware system and can reach up to $\sim 0.5 \text{ ms}/\mu\text{m}^2$ for a LASER on an animal scanner with strong gradients.

Another popular approach to compensate for cross terms consists of acquiring data with diffusion gradients of opposite polarities.^{37,38} The geometric mean of these signals is free from cross terms, although strictly speaking this is only valid in the limit of monoexponential attenuation and under the assumption of homogenous diffusion within the voxel. Another advantage of this method is that it also compensates for any static background gradients that cannot be foreseen. Alternatively, the diffusion-encoding gradient waveforms can be designed to minimize the error due to cross terms.³⁹

In general, the contribution of cross terms should be kept minimal because they can lead to a poorly defined diffusion time and affect the modeling of microstructural features. Note that, besides cross terms, care should be taken to avoid that diffusion gradients cancel out spoiling/coherence pathway selection gradients (which can, for example, be achieved by using different gradient directions).

For SE-based volume selection, the semi-LASER (sLASER) sequence⁴⁰ (for which LASER stands for “Localization by Adiabatic SElective Refocusing”⁴¹) is now generally preferred over PRESS because it is robust to B_1^+ inhomogeneities and offers large RF pulse bandwidth to minimize chemical shift displacement error. Diffusion-weighting gradients can be inserted in a “double bipolar” fashion,¹³ as shown in Figure 3C, thus maximizing diffusion weighting and compensating for eddy currents (EC).

2.1.3 | Sequences for small animal scanners

dMRS sequences tailored for humans can also be used in small animal scanners. However, one can take advantage of rodent scanners’ specificities to alleviate some limitations of human scanner sequences. In particular, stronger gradients and less conservative specific absorption rate limits enable the use of shorter TE and additional RF pulses. This allows a block-based sequence design in which diffusion weighting and localization are independent, resulting in the absence of cross terms (box 2) between diffusion and localization gradients. In practice, the localization is achieved using a full LASER module, whereas the diffusion block is built around nonselective STE³⁵ or SE^{42,43} (Figure 3D). Localization with the a semi-adiabatic DW-SPECIAL sequence (for which SPECIAL stands for “SPin ECho, full Intensity Acquired Localised”) is also possible.^{44,45}

2.1.4 | About water

Water suppression schemes are the same as for conventional MRS acquisition. However, when metabolite signals are too weak in individual transients for estimating scan-to-scan frequency, phase, and amplitude alterations (see section 3), preserving the water signal with a metabolite cycling approach is recommended to observe both water and metabolites.⁴⁶ This is already available for diffusion-weighted-STEAM (DW-STEAM) and DW-sLASER.^{47–49} Another option is to de-optimize water suppression so that some clean residual signal is still visible. Because water signal arising from CSF may contribute substantially at low b -values ($< \sim 1 \text{ ms}/\mu\text{m}^2$) and may not represent metabolite signal distortions properly, it can be suppressed with a water-selective fluid-attenuated inversion recovery module at the start of the sequence^{48,50} while preserving water signal from parenchymal tissues.

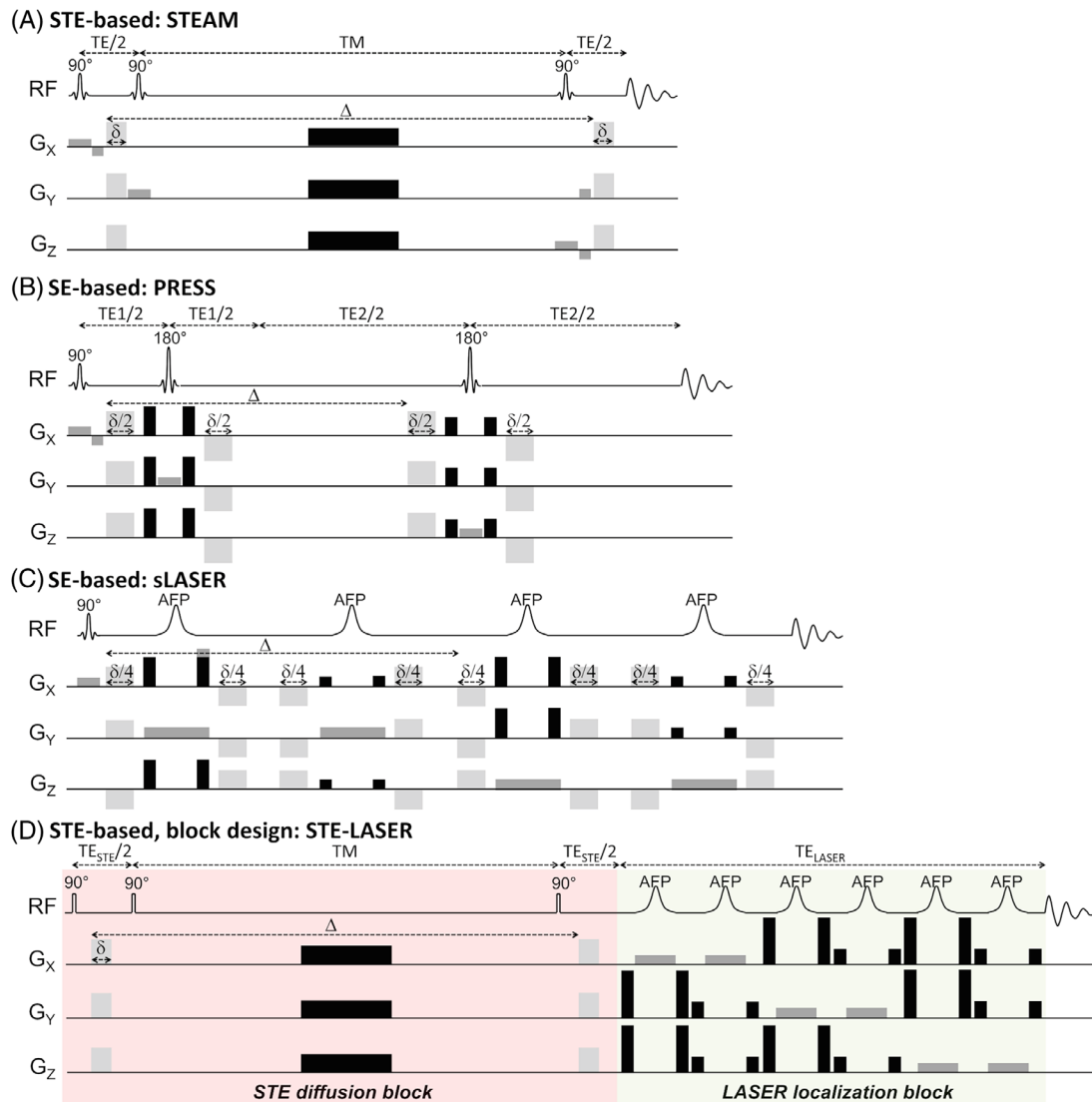


FIGURE 3 Chronograms of typical dMRS pulse sequences. (A) STE-based STEAM, using a pulsed field gradient¹¹; (B) SE-based PRESS, using a bipolar pulsed field gradient scheme³³; (C) SE-based sLASER, using a double bipolar pulsed field gradient scheme³⁴; (D) STE-based block-design STE-LASER, using a pulsed field gradient scheme.³⁵ The STE block (in pink) can be replaced by a SE block. While the first three sequences can be used in humans, the last one is difficult to achieve in humans due to SAR and TE. Figure adapted from Palombo et al.¹⁴ SAR, specific absorption rate; SE, spin echo; sLASER, semi-localization by adiabatic selective refocusing; STE, stimulated echo.

2.2 | Experimental setup and challenges

2.2.2 | Pilot study on phantom

2.2.1 | Optimizing data quality

Methods for acquisition of optimal MRS data have been described in recent consensus papers,^{51,52} and strategies to improve the quality of spectra with motion compensation have been published.⁵³ Nevertheless, in the context of dMRS, some parameters that can influence the diffusion measurements, and that must be managed very carefully, are summarized in Table 2 and detailed below when necessary.

It is strongly recommended to test a newly implemented dMRS sequence on a phantom before acquiring data in vivo. For a standard set of low b -values, it is possible to use a simple agarose phantom (water alone in a phantom is more prone to mesoscopic flows and not ideal, particularly for longer t_d). However, metabolites' diffusion is about 4–5 times slower than that of water, and a water-based phantom cannot be used to assess the quality of a sequence at high b -values ($>3\text{--}4\text{ ms}/\mu\text{m}^2$). Ethylene glycol is a cheap liquid that has a diffusion coefficient at room temperature of about $0.1\ \mu\text{m}^2/\text{ms}$ and a simple NMR spectrum. Its use

TABLE 2 Checklist for a successful dMRS acquisition.

Experimental devices/tools	
Temperature	<i>In animals</i> (*): monitor and maintain stable body temperature
Motion	<ul style="list-style-type: none"> • Store individual transients for correction during processing • <i>In humans</i>: use cardiac-triggering (+ respiratory-triggering for applications outside the CNS) • <i>In animals</i>: use appropriate animal holder
Vibration (gradient-induced)	<i>Suggestions for STE-acquisition</i> : possible to add an additional set of gradients preceding the excitation, and matching the diffusion encoding gradients and diffusion time
Sequence parameters and acquisition management	
Minimal <i>b</i> -value	Ensure minimal gradient strength required for efficient spoiling of spurious echoes
<i>b</i> range	<ul style="list-style-type: none"> • <i>ADC measurement</i>: max <i>b</i>-value ~3–5 ms/μm² • <i>Kurtosis</i>: max <i>b</i>-value ~8–10 ms/μm² • <i>Fully dispersed neurites model</i>: max <i>b</i>-value ~20 ms/μm² (<i>t_d</i> value is also important, cf. section 5) • <i>Bi-exponential analysis</i>: max <i>b</i>-value ~25 ms/μm²
Number of directions	<ul style="list-style-type: none"> • For rotation invariant powder averaging (cf. section 5) <ul style="list-style-type: none"> ◦ Three directions minimum in a gray matter voxel with low FA ◦ 12 directions in a white matter voxel with high FA • For DTS <ul style="list-style-type: none"> ◦ Six directions minimum ◦ Three directions to compute the trace only
Transients (*)	Store individual transients for phase and frequency correction in processing
Voxel size (*)	Large enough to detect one singlet signal (typically tNAA) at <i>b_{max}</i> in single shot (for processing), unless water signal can be used in a metabolite-cycling experiment
Interleaved acquisitions (*)	Mitigates biases due to frequency, shimming, sensitivity drifts, and metabolic variations
Phase cycling	Ensure proper phase cycling across <i>b</i> -values and diffusion encoding directions, in particular if single acquisitions are discarded based on data quality
Additional acquisitions required for processing	
Macromolecules (*)	Acquire MM using inversion recovery + high <i>b</i> -value to eliminate residual metabolite signal
Eddy current correction (*)	Acquire water signal with identical gradient scheme as metabolite scans or when not possible data with opposite gradient polarity

Note: (*) contain more details in the main text. This table only describes what is specific to dMRS in comparison with MRS. The prior is a successful MRS acquisition.

Abbreviations: CNS, central nervous system; dMRS, diffusion-weighted MRS; DTS, diffusion tensor spectroscopy; FA, fractional anisotropy; MM, macromolecules; STE, stimulated echo; tNAA, *N*-acetylaspartate + *N*-acetylaspartylglutamate.

is recommended at high *b*-values.³⁵ On human scanners, it is also possible to use the standard “Braino” phantom⁵⁴ for *b* < 1.6 ms/μm², or a National Institute for Standards and Technology phantom⁵⁵ to access a wider range of diffusivities. A few basic measurements to evaluate in such freely diffusing liquids are:

- A monoexponential decay of the signal as a function of the *b*-value (when changing gradient strength), corroborating the expected diffusion coefficient (at

room temperature, agarose phantom, or water-based phantom: ~2 μm²/ms, ethylene glycol phantom: ~0.1 μm²/ms),

- A constant diffusion coefficient when the *t_d* is changed,
- Isotropy of the above measurements.

If these observations are not matched, the sequence needs to be revised (often pointing toward a miscalculation of the *b*-value and cross terms, see box 2).

2.2.3 | Experimental devices/tools

Animal setup (c.f. table 2)

A stable anesthesia level should be maintained to avoid potential bias.⁵⁶ Animal holders and fixation are excellent tools to minimize motion during the acquisition (Table 2).

2.2.4 | Sequence parameters and acquisition management

Handling signal accumulation via repeated transients (c.f. table 2)

Care should be taken to perform phase cycling instead of having the same phase on all transients (which might be the case by default for some systems when storing individual transients, e.g., when using “number of repetitions” in Bruker’s ParaVision, Billerica, MA, USA) (Table 2).

There is no consensus as to whether the number of transients per b -value should be increased with b -value. There are, however, arguments for doing so, when practically feasible. First, some fitting softwares, such as LCMoDel⁵⁷ (see section 3), will provide more consistent signal quantification if averaged spectra across b -values have a comparable SNR, but more robust fitting tools such as FiTAID with 2D prior knowledge may not require the same consistency. Second, more transients might be corrupted by motion artifacts at high b -values, which will then be discarded during processing. So one may want to acquire more transients to start with. On the other hand, acquiring enough transients at high b -values to match low b -value SNR might be too time-consuming, especially in human applications. Optimized acquisition schemes can be further tested with simulations depending on the application, the fitted model, the available time for the acquisition, etc. Some authors have already proposed optimized b -value schemes for an accurate estimation of NAA diffusion coefficient in the corpus callosum, using coefficient of variation as a criterion, although without considering a varying number of transients per b -value.⁵⁸

VOI size (c.f. table 2)

Volume of interest (VOIs) should be carefully adjusted to yield just the minimally acceptable SNR in the region of interest, typically to allow for the main metabolite peaks to be visible on individual transients at the highest b -value to allow for efficient frequency and phase correction (see section 3). However, too large a voxel may result in artifactual signal attenuation due to bulk rotation. Indeed, for a given rotation angle, the absolute displacement at the extremity of the voxel is larger for a larger voxel, hence resulting in larger phase variation. More quantitatively, it can be shown that, for short diffusion gradients and small

rotation θ of the sample during the diffusion time, signal loss scales like the sine cardinal (sinc) of $L*\theta$, where L is the voxel size along the direction perpendicular to diffusion gradient (Table 2).

Cardiac triggering

Whereas small translational motion can be corrected for by adjusting individual frequency/phase shifts during processing (see section 3) or by using prospective motion correction methods,⁵³ the effect of physiological motion (cardiac/CSF pulsation) might result in amplitude drops, particularly in humans at high b -values^{59,34} and for VOIs located close to the ventricles. The use of cardiac triggering with an optimal trigger delay in combination with retrospective processing correction (see subsection 3.2.) allows to minimize bias. Fluid-attenuated inversion recovery to null water signal from CSF when using metabolite cycling is not feasible in combination with triggering. Similarly, cardiac triggering places limits on the length of the water suppression module and may also cause TR to be different from transient to transient and increase acquisition time. In body applications, both cardiac and respiratory triggering might be necessary.

Water suppression

Diffusion weighting is rather helpful regarding water suppression. Because water diffuses faster than metabolites, diffusion gradients strongly attenuate the water signal. However, when the TM is very long (typically to study $t_d > 500$ ms), the water suppression might degrade. Although the water signal should be completely crushed before excitation, if a small amount of water was not crushed properly, this residual signal will relax during the TM. The crushers scheme must be carefully optimized, but it is sometimes challenging. In practice, adding a water suppression pulse during the TM can help crush the residual signal when using a long TM.⁶⁰

2.2.5 | Additional acquisitions required for processing

Macromolecules

For a TE shorter than ~ 80 – 100 ms, contributions of macromolecules (MM) cannot be neglected,⁶¹ especially at high b -values in which contributions of MM become more prominent relative to metabolites due to slow MM diffusion (Figure 4 in 17). It is recommended to acquire an experimental MM spectrum for subsequent unbiased quantification of metabolites (see section 4). This is achieved using metabolite-nulling by inversion-recovery (or double inversion recovery).⁶² Suppression of residual metabolite signal can be further improved by performing

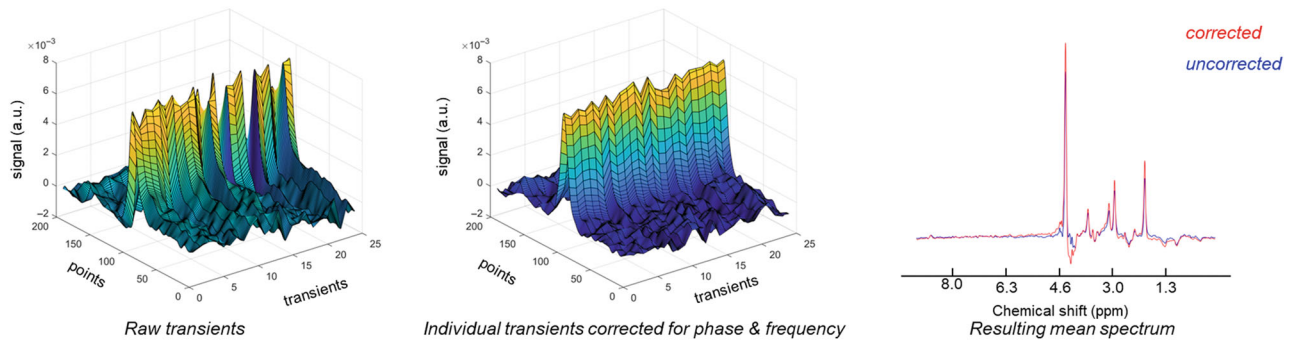
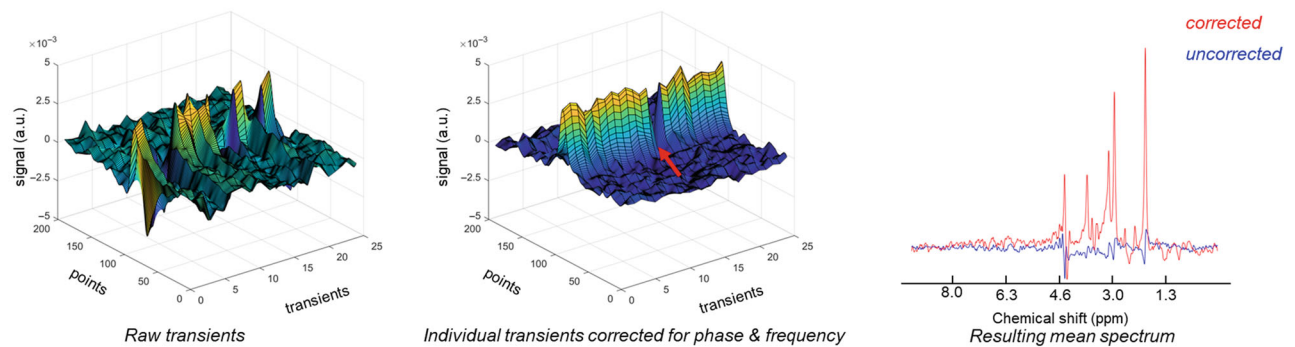
(A) Example of phase and frequency correction for $b \sim 0.6 \text{ ms}/\mu\text{m}^2$ (B) Example of phase and frequency correction for $b \sim 4 \text{ ms}/\mu\text{m}^2$, with one outlier (red arrow)

FIGURE 4 Examples illustrating the importance of phase and frequency correction at (A) $b = 0.6 \text{ ms}/\mu\text{m}^2$ and (B) at $b = 4 \text{ ms}/\mu\text{m}^2$.

the acquisition at high b -values (typically $10 \text{ ms}/\mu\text{m}^2$)⁶³ or as described in Ref. 61 but always using the specific dMRS sequence for acquisitions. MM signals can also be used as an endogenous sensor for motion⁶⁴ (see section 3).

Eddy current correction

Eddy current correction (ECC) may be required, in particular on human scanners when high gradient strength is used. ECC relies on measuring the temporal phase of the water signal.⁶⁵ Hence, unless metabolite cycling is used, non-water-suppressed spectra must be acquired as reference for all diffusion conditions requiring ECC. In that case, it is important that the water signal dominates these reference scans. Note that this is not always possible at high b -values due to faster water diffusion, unless the water-suppressed spectrum is subtracted from the non-water-suppressed spectrum.⁶⁶ An increased number of transients also ensures a high-water SNR: A noisy reference scan used for ECC will introduce artifacts during processing. In applications in which water peak-based ECC is not possible, suppression of EC effects may be feasible using a bipolar diffusion-encoding scheme under the assumption of a linear system response in which EC effects cancel out for opposite readout polarities.^{28,67}

3 | PROCESSING STEPS SPECIFIC TO DMRS DATA

dMRS and general MRS data processing share most steps. Because an excellent consensus paper already exists on MRS processing,⁶⁸ the objective of this section is to emphasize where additional care is required for dMRS. A robust and accurate processing is particularly important for dMRS. Indeed, the estimation of diffusion measures like ADC relies on the measurement of the attenuation of the signal across multiple acquisitions (each with different diffusion-weighting conditions) and is thus prone to error propagation. For example, a 5% underestimation of the signal of a given metabolite at $b = b_0 + 3 \text{ ms}/\mu\text{m}^2$ will lead to a 15% overestimation of its ADC in a typical measurement setup ($\text{ADC} \sim 0.12 \mu\text{m}^2/\text{ms}$; 30% expected signal attenuation between b_0 and $b_0 + 3 \text{ ms}/\mu\text{m}^2$). At lower b -values (e.g., $b_0 + 1 \text{ ms}/\mu\text{m}^2$), the same error on metabolite quantification can lead to a 42% overestimation of the ADC. Although precision is better at higher b -values, the accuracy of ADC estimation is corrupted by kurtosis from $b = 3\text{--}5 \text{ ms}/\mu\text{m}^2$ (see subsection 5.2). Moreover, diffusion gradients make diffusion-weighted spectra even more sensitive to the subject's motion and scanner instabilities. Processing can help mitigate the effect of small

bulk or physiological motion artifacts, which results in frequency/phase drifts (translational motion) and amplitude fluctuation (rotation, compressive motion).¹⁶ An overview of the current toolboxes available for processing (and fitting; see section 4) dMRS data is provided in Table 3.

The dMRS community tends to use custom-made Matlab (MathWorks, Natick MA) routines, passed on and incrementally modified by users. From a survey carried out during the 2021 Lorentz Center workshop (Leiden, the Netherlands), most pipelines contained the recommended processing steps detailed in this section. Although some of these pipelines are shared along with publications on a git platform, they are not necessarily easy to find for newcomers. In Table 3, we provide a summary of the available toolboxes/packages that can be used for dMRS data processing. Because the functions to be used might vary with package updates, more details about how to use these packages for dMRS processing can be found in the dMRS section on MRShub (<https://forum.mrshub.org/t/processing-for-dw-mrs/935>).

3.1 | dMRS specificities for processing steps shared with conventional MRS

For the following steps, the reader can refer directly to Ref. 68:

- RF coil combination (3.2.1 in Ref. 68)
 - The amplitude, phase, and noise terms necessary for coil combination can generally be determined from the b_0 unsuppressed water data for dMRS.
- Phase and frequency drifts correction (3.1.3 in Ref. 68)
 - The effect of phase and frequency correction is particularly important at high diffusion weighting when the phase shift between scans is larger (Figure 4).
- Outlier removal (3.1.2, Table 2, and Figure 4 in Ref. 68).
 - The outlier removal must be carried out at a given set of b -value and direction. If more than 30% of the transients are affected, it is advised to discard the dataset. See subsection 3.2.
 - After the individual transients are averaged and sorted, it is still possible that the resulting spectrum is corrupted by motion. See subsection 3.3 for further motion detection.
- ECC (see section 2)
 - When water data at high b -value are too noisy for ECC, an alternative (during processing) is to decouple the water signal from the noise with a singular value decomposition (SVD) and use the synthetic FID for the ECC.

3.2 | Specific considerations for a metabolite-cycling approach

With a metabolite-cycling approach (see section 2), the nonsuppressed water signal can be beneficial for compensating motion-related signal loss.⁴⁸

Because this technique does not use water suppression, it is susceptible to sideband artifacts⁸⁰ that can affect spectral quality if any hardware component is malfunctioning and fluctuating, for example, with the power source. Therefore, spectra should be carefully inspected for artificial resonance peaks, which appear at the base modulation frequency or its higher harmonics (e.g., multiples of 50 Hz). However, due to its 10,000-fold higher SNR, water is a particularly useful internal reference not only to improve coil-channel averaging, phase, and eddy current correction but also to compensate for signal loss due to motion.⁴⁸ This motion compensation is based on the assumption that a certain quantile of transients at a given b -value remains unaffected by motion (e.g., 25% quantile of transients) and thus can serve as an internal reference for rescaling motion-induced decay/dephasing. When using cardiac triggering (see section 2), the effective TR may vary across transients and thus induce T_1 -related amplitude fluctuations between b -values if not taken into account. It is then suggested to apply a correction factor ($1 - \exp(-T_{\text{Reff}}/T_1)$) prior to defining the reference level.⁸¹

Note that motion compensation may fail when all transients are compromised by motion (e.g., if only a small number of transients is acquired, if all transients are similarly distorted due to table vibrations, or if at extremely high b -values the water has decayed to the level of metabolite amplitudes).

3.3 | Specific considerations for short TE dMRS: macromolecules

Acquisition of a MM spectrum is briefly described in section 2, and more detailed information can be found in Ref. 61. Some MM spectra are openly available (https://mrshub.org/datasets_mm/). For dMRS, some specific details about MM should be considered: At very high b -values, MM account for half of the signal (Figure 4 in Ref. 17). In vivo MM should be acquired with the same sequence as the dMRS signals using a single or double inversion recovery module. The MM signal that is used for fitting needs a very low noise level, and experts in the field use two different methods: acquiring a very high number of MM spectra until the noise level is barely detectable; or fitting the average MM spectrum⁸² and including the resulting fit (noise-free by default, but requires confidence in the fit) in the basis set.

TABLE 3 Available packages referenced on MRShub to process and/or fit MRS data.

	Processing				Fitting				Open source	Free	Language	Reference
	Coils Combination	Phase and frequency correction	ECC	Water residual removal	Basis set generation	Sequential	2D	Signal fitting				
ABfit	X	X	X	X	X	✓	X	✓	✓	R	Wilson, 2021 ⁶⁹	
AQSES	X	✓	✓	✓	X	✓	X	✓	✓	Java	Pouillet et al., 2007 ⁷⁰	
FID-A	✓	✓	✓	✓	✓	X	X	✓	✗	Matlab	Simpson et al., 2017 ⁷¹	
FitAid	X	X	X	X	X	✓	✓	X	✓	Java	Chong et al., 2011 ⁷²	
FSL-MRS	✓	✓	✓	✓	✓	✓	✓	✓	✓	Python	Clarke et al., 2021 ⁷³	
jMRUI 6*	X	✓	✓	✓	✓	✓	X	X	✗	Java	Stefan et al., 2009 ⁷⁴	
LCModel	X	X	✓	X	X	✓	X	✓	✓	Fortran	Provencher, 1993 ⁵⁷	
Osprey	✓	✓	✓	✓	✓	✓	X	✓	✗	Matlab	Oelzschner et al., 2020 ⁷⁵	
ProFit-1D & SpectroS	✓	✓	✓	✓	✓	✓	X	✓	✗	Matlab	Borbath et al., 2021 ⁷⁶	
spant	✓	✓	✓	✓	✓	✓	X	✓	✓	R	Wilson, 2021 ⁷⁷	
Tarquain	✓	✓	✓	✓	✓	✓	X	✓	✓	C++	Wilson et al., 2011 ⁷⁸	
Vespa	✓	✓	✓	✓	✓	✓	X	✓	✓	Python	Soher et al., 2011 ⁷⁹	

Note: Packages highlighted in dark gray are routinely used by dMRS users. An orange tick mark means that the package is freely available but relies on a licensed language. A package is considered open source when a shared repository exists. *jMRUI 7.0 is to be released soon, with FitAID as a plugin. **for Osprey, the basis set generation comes from the online tool MRSCloud. The updated version of this table can be found on MRShub dMRS forum (<https://forum.mrshub.org/t/processing-for-dw-mrs/935/2>).

Abbreviation: EC, eddy currents.

MM can also be used as an internal probe for residual motion effects for averaged spectra (per DW condition). MM have a very low ADC ($\sim 0.005\text{--}0.01\ \mu\text{m}^2/\text{ms}$); hence, their signal is virtually unaffected by diffusion weighting. To evaluate residual motion effects, one can visually inspect stack plots of spectra (before fitting) for gross signal drop or assess changes in MM signal by integrating its peak at 0.9 ppm. This can be done prior to fitting by inspecting visually stack plots of spectra for gross signal drop or by integrating the MM peak at 0.9 ppm.⁶⁴ If the MM fit is reliable, it can also be done after spectral fitting by measuring the MM ADC. The MM decay is monoexponential up to very high b -values.³⁵

4 | SPECTRAL FITTING FOR ESTIMATING METABOLITE DIFFUSION PARAMETERS

Quantitative information is extracted from an acquired MR spectrum by fitting a physics-informed model to it. The expert consensus recommends the use of linear-combination modeling, usually based on nonlinear least-squares optimization, for most in vivo MRS applications,⁶⁸ and is also recommended for dMRS. The objective of this section is to discuss and emphasize aspects of spectral fitting of particular importance to dMRS, and suitable methods to incorporate diffusion modeling into the spectral fitting process. Along with a careful processing (c.f. section 3), a well-designed fitting pipeline can mitigate critical issues routinely encountered with dMRS such as motion dephasing, lineshape distortions, eddy currents, and frequency drift.⁸³

4.1 | Basis sets and macromolecular signals

Diffusion weighting changes metabolite-specific signal amplitudes, not J-evolution. Thus, metabolite basis sets are unaffected by diffusion encoding and can be simulated as for conventional MRS.⁶⁸ Note that for spin echo sequences, longer TEs required to achieve strong diffusion weighting will exhibit greater fit uncertainty due to low SNR, particularly for overlapping metabolite signals.⁸⁴ To ease the fitting of dMRS data, predefined basis sets are increasingly made publicly available and will be collected and curated by the MRS community (MRS Hub, basis-sets [https://mrshub.org/datasets_basissets/]). When these predefined basis sets are used, one has to take care to select those matching the dMRS sequence and TE.

For TE < 80–100 ms, it is advised to include an experimentally measured MM pattern in the basis set (c.f. section 2).⁶¹ If experimentally measured MM are not

available, the MM signals should be modeled with parameterized individual MM components (e.g., MM09, MM12) that are included in many contemporary fitting algorithms. To reduce the degrees of freedom and prevent variability of final ADC estimation, the parameterized MM should be derived at the highest b -value and kept constant in shape for the other diffusion weightings.

4.2 | Sequential and simultaneous spectral fitting

DW spectra span an interrelated 2D space defined by the spectral (time/frequency) and diffusion (dephasing) dimension. Both dimensions have to be addressed: (i) The spectral dimension is decomposed into contributions from individual metabolite patterns (basis sets) by linear-combination modeling⁶⁸; (ii) the signal decay along the diffusion dimension is fitted to the metabolite amplitude estimates, either using an abstract diffusion signal representation (e.g., mono-/biexponential, kurtosis, diffusion tensor spectroscopy) (see subsection 4.2.1.) or a signal model directly related to tissue microstructure (e.g., cylinders, spheres, multi-compartment)⁸⁵ (see section 5). To achieve accurate fitting along the diffusion dimension, correct b -values should be calculated, including slice-selective and crushing gradients, and cross terms (c.f. box 2).

With recently available software, a dMRS dataset can be fitted either in a *sequential* (1D) or *simultaneous* (2D) mode. In sequential mode, fitting along the diffusion dimension is performed in a separate post hoc optimization after *sequential (traditional) spectral fitting*, whereas *simultaneous fitting* explicitly incorporates the diffusion model into the spectral fitting process. *Simultaneous fitting* is not yet a subject of consensus or recommendation but is a very promising approach; hence, the underlying concepts are introduced in this part.

4.2.1 | Common signal representations

There are different diffusion signal representations possible, depending on the acquisition parameters (b -values sampled, maximum b -value used in an experiment [b_{max}], number of directions). It has become established practice to use a monoexponential representation for $b \leq 5\ \text{ms}/\mu\text{m}^2$, a kurtosis or biexponential for $b \leq 10\ \text{ms}/\mu\text{m}^2$, and a biexponential for $b > 10\ \text{ms}/\mu\text{m}^2$.³⁵ ADC values calculated using a monoexponential representation across different species and different diffusion times are summarized in Valette et al.⁸⁶ The RMS error of the residuals of the biexponential fit for a specific metabolite can serve as a predictor for its SD from a Gaussian noise model. It is a useful

measure to determine whether or not a microstructural model is applicable (C.f. section 5). However, it is important to note that the fast and slow diffusion components cannot be interpreted as individual cellular compartments. If at least six directions are acquired, it is also possible to compute the diffusion tensor from each monoexponential decay.⁸⁷ For the MM, a monoexponential representation is usually sufficient, although at very high b -values this assumption may start to break down.³⁵ These representations describe diffusion using only a few parameters (two for monoexponential, three for kurtosis, and four for biexponential), which prevents overfitting (although introducing constraints on metabolite diffusion, which can affect tissue modeling).

4.2.2 | Sequential (1D) fitting

In *sequential fitting*, the spectrum arising from each separate diffusion encoding (b -value, direction, t_d , or encoding scheme) is fitted independently. Most fitting tools include baseline estimation (e.g., adding a smooth spline or polynomial), and the baseline flexibility is a major contributor to uncertainty and variance in the fitting process.^{34,88–91,69} Therefore, care should be taken to prevent the baseline from introducing additional variability and systematic differences into the estimates of metabolic diffusion properties at different b -values. It is advisable to not over parameterize the baseline and keep it similar between b -values with the same number of spline knots or low-degree polynomials (e.g., to include residual water artifacts). If possible, relative metabolite frequency shifts in individual spectra should be constrained to a minimum to prevent inconsistent models at different b -values and limit the degree of freedom of the overall fitting process.

Fit results for metabolites with similar spectral patterns are difficult to reliably separate, and it is common practice to indicate the total combined estimated area for correlated groups of metabolites (e.g., $tNAA = NAA + NAAG$, $tCr = Cr + PCr$, $tCho = PCho + GPC$). Separate estimates of strongly overlapping signals will have lower precision. The use of such sums in diffusion analysis implies that the diffusion properties of the constituents are comparable; however, that is not at all a given, either because the molecules are of substantial difference in size and molecular weight (e.g., PCho and GPC, and Cr and PCr) or cellular location (e.g., glutamine) and Glu). If the diffusion properties are expected to be similar, it may be beneficial to use soft constraints to regularize the relative concentration ratios of such connected metabolites to a predefined value to obtain more consistent results and prevent overfitting. If diffusion properties differ, this approach will fail.

After sequential spectral fitting, the diffusion-weighted individual metabolite amplitude estimates or their sums (one per diffusion encoding) can be fitted using a signal representation or a tissue model.⁸⁵

4.2.3 | Simultaneous (2D) fitting

In *simultaneous fitting*, all spectra from all diffusion encodings are fitted in a single step.⁸³ Spectral parameters are adapted for each b -value, direction, t_d , or encoding scheme under the constraints of separate priors on the selected diffusion model for each metabolite or for the MM. For example, in an experiment with increasing b -value, amplitude decays for each metabolite could be constrained to a (multi-)exponential decay function along the diffusion dimension. As in general, simultaneous fitting constraints can be applied to width, phase, or relative frequency parameters to be consistent for the whole data set—although care should be taken not to overconstrain the model given that lineshapes may alter based on EC (possibly not fully compensated and thus dependent on diffusion gradient strengths). Simultaneous fitting allows to introduce assumptions on equal diffusion behavior for multiple metabolites to stabilize the fits at each b -value (e.g., equal ADCs for metabolites like *scyllo*-inositol and Ins, or monoexponential decay for the MM, or even more complex models for particular metabolites). Moreover, the use of concentration ratio constraints for overlapping metabolites with differing diffusion properties is feasible and may promise to help segregation of metabolite patterns with differing diffusion properties (although without sufficient SNR, spurious effects from overfitting could still result when allowing parameters to adapt). Simultaneous fitting likely also aids baseline estimation (by constraining its parametrization to a specific decay model) and lineshape parametrization (which is difficult at high b -values due to low SNR).⁸¹

The biexponential representation is good to stabilize *simultaneous fitting* for $b > 10 \text{ ms}/\mu\text{m}^2$ because it represents the signal well, is easy to implement, and has a minimum number of free parameters. It is useful when fitting diffusion properties of J-modulated or low concentration metabolites like Glu, Ins, or glucose). Indeed, a recent study on a set of synthetic dMRS spectra found a more reliable estimate of diffusion and tissue properties when simultaneous fitting is applied.⁹² This is supported by Tal et al.,⁹³ showing that *simultaneous 2D fitting* improved precision by at least 20% compared to 1D fitting.

Moreover, simultaneous fitting can incorporate additional shared information between individual or averaged transients, such as line broadening and shape, phase (zero and first order), diffusion-orientation, spectral editing, or relaxation. This can reduce fitting uncertainties;

mitigates signal distortions; and enhances robustness of, for example, multiparametric dMRS.^{83,94} Nevertheless, a crucial challenge remains to establish and validate dynamic models to ensure unbiased results.⁹⁴

4.3 | Comparability of results between fitting algorithms and methods

It should be noted that the fitting of *in vivo* MRS data represents a complex, ill-posed optimization problem, and there are many available algorithms to solve it. Recent studies have revealed that fitting results can vary substantially not just between fitting algorithms^{89,95,96} but also within any given algorithm,^{95,96} depending on highly sensitive fit options and settings. Preliminary evidence from the 2021 dMRS workshop suggests that dMRS is no exception to this, and given the strong impact of error propagation on the estimated ADC, achieving optimal spectral fitting performance and continued comparison across methods is critical. As the field of dMRS develops, it will be important to benchmark and validate emerging fitting methods, ideally against synthetic data with known ground truth.

5 | MODELING: LINKING THE DIFFUSION PROPERTIES TO TISSUE MICROSTRUCTURE

In this section, we will focus on the consensus and recommendations regarding the biophysical modeling of purely intracellular metabolites to infer histologically meaningful descriptions of brain microstructure from dMRS. We highlight three points of consensus that set out the currently accepted minimal model of metabolites' diffusion in brain tissue. We then provide guidelines on how to adapt this minimal model to typical experiments.

5.1 | The minimal model of metabolite diffusion in brain tissue: randomly oriented infinitely long straight cylinders

The randomly oriented infinite cylinders model is a simple analytical model of diffusion in infinitely long (i.e., diffusion is only restricted in transverse directions) and randomly oriented cylinders (i.e., reflecting mesoscopic isotropy). This section describes why it is a reasonable biophysical model to extract microstructural information from brain metabolite diffusion, and the conditions that need to be fulfilled for it to be applicable. Specific

experimental conditions (e.g., pathology, development) might affect the relevance of this model.

5.1.1 | Intracellular brain metabolites exhibit non-Gaussian diffusion

At high *b*-values and for typical diffusion lengths of 5–15 μm , the dMRS signal from intracellular brain metabolites exhibits non-monoexponential decay (Figure 5A). This provides a hint about the length scale of structures hindering metabolite diffusion (a few μm). Monoexponential behavior breaks for *b*-values $>3\text{--}5\text{ ms}/\mu\text{m}^2$. This has first been observed with early measurements of NAA diffusion in brain cells at various t_d and to high *b*-values (up to $b = 30\text{ ms}/\mu\text{m}^2$).⁹⁷ Other intracellular metabolites exhibit similar non-monoexponential decays, as reported in subsequent studies.^{35,98} Multi-exponential (usually bi-exponential) signal representations sometimes used to characterize the signal decays at high *b*-values do not inform about cytoarchitecture. Biophysical models are thus built to extract meaningful cytoarchitectural parameters.

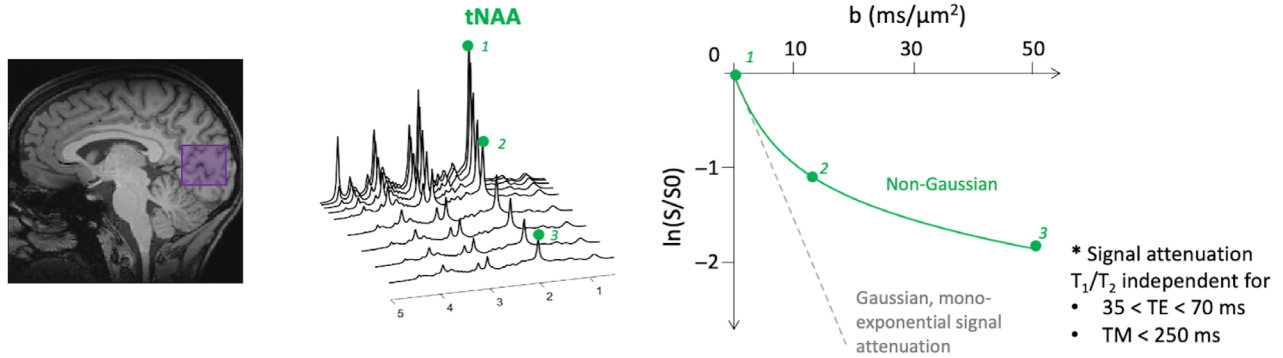
5.1.2 | Correlation between relaxation and diffusion properties is negligible for intracellular brain metabolites

Correlation between diffusion and relaxation properties may arise from the presence of different compartments, each with its own relaxation times and diffusion properties (e.g., cytosolic versus mitochondrial compartments). The studies summarized in Table 4 suggest that for $35 \lesssim \text{TE} \lesssim 70\text{ ms}$, $\text{TM} \lesssim 250\text{ ms}$ and $t_d \lesssim 250\text{ ms}$, minimal to no correlation between relaxation and diffusion properties exist for intracellular brain metabolites (Figure 5A). Therefore, the diffusion measurements performed within this regime carry information about the cellular microarchitecture, unbiased by the inherent relaxation processes. This also suggests that experiments performed within this experimental regime should yield comparable results across studies.

5.1.3 | Purely intracellular brain metabolites exhibit signatures of microscopic anisotropy

The non-Gaussian nature of metabolite diffusion can have different origins. Experimental evidence supports the hypothesis that one of the major sources is the microscopic fractional anisotropy (μFA) of the brain microstructure. Microscopic anisotropy represents the level of anisotropy

(A) Intracellular brain metabolites exhibit non-Gaussian diffusion and correlation with relaxation properties is weak.*



(B) Micro-anisotropy of intracellular brain metabolites is high and their diffusion properties match with diffusion in elongated fibres.

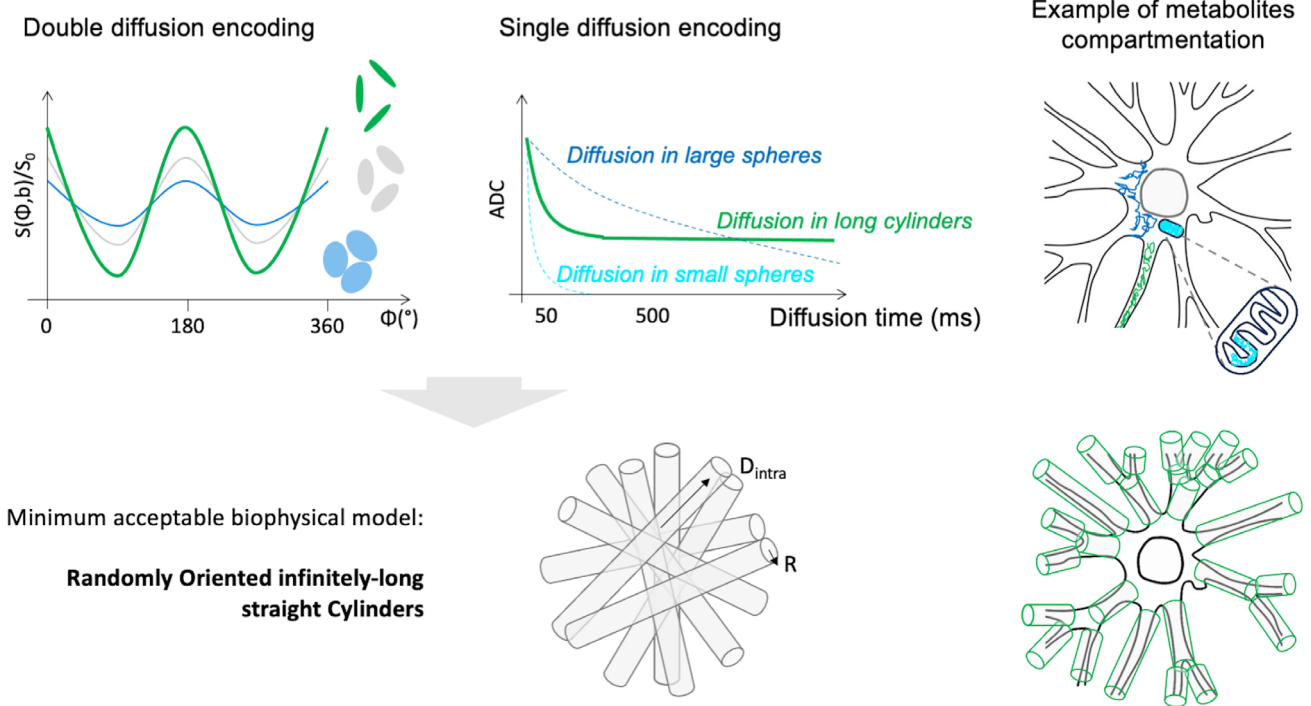


FIGURE 5 (A) Intracellular metabolites exhibit non-Gaussian diffusion, and correlation with relaxation properties is weak. The gray curve (right panel) represents the logarithm of the normalized signal decay in the case of Gaussian diffusion (e.g., free diffusion). The green curve (right panel) represents the logarithm of the normalized signal decay, coming from tNAA. The data were simulated for the Lorentz workshop pregame and are available on github (<https://github.com/dwrmrshub/pregame-workshop-2021>). Data always originates from large voxels, as exemplified in the left panel. (B) Intracellular brain metabolites μ FA is high, and their diffusion properties match with diffusion in elongated fibers. (Left, green curve) Intracellular metabolites exhibit a strong modulation with the angle Φ between diffusion directions in DDE-MRS experiment, reflecting a high μ FA. (Right, green curve) Their ADC from very short to very long t_d is well represented by diffusion in long cylinders (right, gray curves) in contrast to diffusion in spheres. (Bottom) The randomly oriented infinite cylinders model is characterized by the diffusivity D_{intra} along the cylinder and the radius R . If t_d is too long and/or b_{max} is too low, the acquisition does not support the estimation of the radius R , and the model can be simplified to randomly oriented sticks, with D_{intra} as the only parameter. D_{intra} , intracellular diffusivity; DDE, double diffusion encoding; μ FA, microscopic fractional anisotropy; tNAA, *N*-acetylaspartate + *N*-acetylaspartylglutamate; t_d , diffusion time.

TABLE 4 Summary of studies reporting potential dependence between the TE used and the measured diffusion properties.

Publications	B ₀ field & Sample	TE range (ms)	t _d (ms)	Conclusions
Assaf & Cohen, 1998 ⁹⁹	11.7T Ex vivo rat brain	70–200	35 & 95	NAA bi-exponential fit depends on TE
Assaf & Cohen, 1999 ⁹⁷	11.7T Excised bovine optic nerve	70–550	125	NAA signal decay depends on TE
Branzoli et al., 2014 ¹⁰⁰	7T In vivo human brain	40–160	44–246	No TE dependence for TE < 90 ms (except tCr at t _d = 246 ms).
Ligneul et al., 2017 ³⁵	11.7T In vivo mouse brain	33–73	20–253	No TE dependence for ADC or ADCs of fast and slow components (from bi-exponential fit)
Mougel et al., 2022 ¹⁰¹	11.7T In vivo mouse brain	50–110	20	No TE dependence for ADC and Kurtosis (except very small ADC variation for tCr)

Abbreviations: tCr, tCr, Cr + phosphocreatine; t_d, diffusion time.

at the microscopic scale (i.e., in the range of the diffusion length probed, 5–15 μm) and not at the (macroscopic) voxel size scale (known in dMR as *fractional anisotropy* [FA]). For instance, if metabolites were mostly located in round cell bodies, the measured μFA and FA would be close to 0. On the other hand, if they were mostly located in thin and elongated fibers, randomly oriented within the spectroscopic voxel, then measured μFA would be close to 1, but FA would still be close to 0.

Several studies using single diffusion-encoding acquisitions and high *b*-values have demonstrated that the diffusion of intracellular metabolites exhibits signatures of microscopic anisotropy, both in rodent gray matter (GM)^{102,103} and in human white matter (WM).¹⁰⁴ More recently, from powder-averaged data acquired at high *b*-values, it has been measured that the μFA of NAA nears 1 in human WM.¹⁰⁵ A few works exploring metabolite ADC over a wide range of t_d also suggest that metabolites are primarily located in elongated fibers.^{6,86,106}

Double diffusion encoding (DDE) acquisitions are challenging but provide more direct measures of μFA. General considerations for DDE in dMRI and dMRS have been covered in recent reviews.^{107,108} Pioneering DDE studies reported high μFA for all intracellular metabolites^{42,109} but slightly higher for NAA (a neuronal metabolite) than for Ins (a glial metabolite). More recent work reports similar results both in the rodent and the human brain.^{110,111}

The diffusion of intracellular metabolites is anisotropic at the microscopic scale in both GM and WM and should therefore represent a key component for any biophysical model of metabolite diffusion (Figure 5B).

5.1.4 | Randomly oriented infinite cylinders model

The previous sections set out the reasons why the randomly oriented infinite cylinders model is a reasonable “minimal” biophysical model for brain metabolite diffusion. It effectively mimics the geometry of cellular processes (neuronal and glial), which is where metabolites are primarily located (only being minimally located in cell bodies).

- *Analytical expression:* The signal attenuation *K* from a given cylinder with orientation **n** by a diffusion gradient pair with orientation **g** can be written as a function of the acquisition parameters (**g**, Δ, δ) and the model parameters *D*_{intra} (intracellular diffusivity) and *R* (cylinder radius), either using the short gradient pulse approximation¹¹² or the van Gelderen’s formula in the case of longer pulses.¹² The orientation distribution of the cylinders can be then factored out by averaging the signal over a reasonably large number of diffusion directions, the so-called directional average or powder-average, *S*:

$$S(\mathbf{g}, \delta, \Delta; D_{\text{intra}}, R) = \frac{\int_0^\pi \sin(\theta) K(\mathbf{g}, \theta, \delta, \Delta; D_{\text{intra}}, R) d\theta}{\int_0^\pi \sin(\theta) d\theta},$$

leaving *D*_{intra} and *R* to be estimated. Here, θ is the angle between the direction of the cylinder’s main axis **n** and the direction of **g**.

- *Open-source implementations of the randomly oriented infinite cylinders model:* Widely used in the dMRI community, several toolboxes contain implementations

of this model (e.g., MISST [<http://mig.cs.ucl.ac.uk/index.php?n=Tutorial.MISST>], DMIPY [<https://github.com/AthenaEPI/dmipy>]). A list of these packages and examples of simple scripts can be found on MRS hub (<https://forum.mrshub.org/t/modeling-dw-mrs-data/943>). We also list educational resources to help get a feeling of the contributions of different parameters (e.g., DIVE [<https://git.fmrib.ox.ac.uk/fsl/DIVE/-/blob/master/README.md>]).

5.1.5 | Conditions of applicability

- *TE regime*: As described in 4.1.2, for data acquired with $35 \lesssim TE \lesssim 70$ ms at $7T \leq B_0 \leq 11.7T$, it is possible to ignore T_2 effects. Due to T_2 dependence to magnetic field, for $B_0 \leq 3T$ the upper bound on TE is expected to be higher; for $B_0 \geq 11.7T$ the lower bound on TE is expected to be higher.
- *Number of directions*: The number of directions needed to achieve a rotation invariant powder averaging increases with the term $b \cdot D_{\text{intra}}$ ¹¹³ and with macroscopic anisotropy in the voxel. In mostly isotropic voxels (e.g., in the rodent GM), as few as three directions might be sufficient.¹¹³ In a very anisotropic voxel (such as in high FA human WM), with ideal SNR conditions a total of 12 directions should provide a rotational invariance up to very high b -values. However, in practice other noise sources might dominate when fewer than 12 directions are used, even in isotropic voxels.¹⁰⁵
- *Limitations and considerations on t_d* : For SE-based pulse sequences (see section 2), the minimum t_d and TE are often constrained by the gradient duration and must be kept constant unless t_d -dependence is explored. t_d -dependence goes beyond the scope of this paper and requires different modeling. To gain higher sensitivity to fiber radius R , shorter t_{ds} are preferred.

As general guidelines for the randomly oriented infinite cylinders analysis, we recommend designing the acquisition to reach a maximum b -value of ~ 20 ms/ μm^2 , keeping TE and t_d constant and as short as possible.

For typical $t_d \sim 40$ – 80 ms, the effect of branching (i.e., metabolites exchanging between cell ramifications) is negligible, and exchange between soma and cellular fibers might be negligible.^{6,114} However, cytoarchitectural features with a characteristic length scale comparable to a diffusion length along fibers (5 – 10 μm) might impact D_{intra} estimated by the randomly oriented infinite cylinders model. These features could be¹¹⁵:

- *Spines*, occurring at ~ 1 – 2 spines/ μm ,
- *Undulations*, occurring over a wavelength $\lesssim 10$ – 16 μm ,

- *Beading/fiber diameter variations* occurring over a length scale of 5 – 8 μm .

The impact of restriction due to *somas* of radius 12 μm might also be nonnegligible.¹¹⁴

For $t_d \gtrsim 100$ ms, *branching* affects the diffusion properties,^{6,114} and sensitivity to the radius extracted from the randomly oriented infinite cylinders model is reduced because the diffusion length relative to the radius is too big ($4t_d D_{\text{intra}} \gg R^2$). Likewise, in cases of low b_{max} (b -value $\ll t_d/R^2$, e.g., b -value $\ll 10$ ms/ μm^2 for fiber $R = 2$ μm and $t_d = 40$ ms) or low SNR, the signal attenuation cannot be used to extract the fiber radius from a randomly oriented infinite cylinders model (see subsection 5.2). A model of randomly oriented sticks should be considered instead (i.e., cylinders with zero radius):

$$K(b, \theta; D_{\text{intra}}) = \exp[-bD_{\text{intra}} \cos(\theta)^2].$$

The powder-average signal can then be expressed as:

$$S(b, D_{\text{intra}}) = \sqrt{\frac{\pi}{4bD_{\text{intra}}}} \operatorname{erf}\left(\sqrt{bD_{\text{intra}}}\right),$$

where *erf* denotes the error function. If the sticks' orientations are uniformly distributed on the sphere (i.e., FA = 0), the ADC along any arbitrary direction derived from low b -values is then $D_{\text{intra}}/3$.

- *Modified randomly oriented infinite cylinders model for very anisotropic voxels* (e.g., WM): The randomly oriented infinite cylinders model is based on the assumption that, within a large spectroscopic voxel, the cellular processes (i.e., neurite and glial processes) are randomly oriented. This condition is usually met for GM voxels or when using enough diffusion directions to yield a reliable powder average. However, it may not be met when using few diffusion directions in voxels located primarily within WM tracts, where the preferential orientation of the cell processes may significantly impact the measured diffusion signal. In this case, the randomly oriented infinite cylinders model should be modified to account for the specific orientation distribution of fibers within the spectroscopic voxel.

The simplest way to do so is to acquire dMRI data suitable for diffusion tensor imaging (DTI) analysis together with the dMRS data and estimate the distribution of principal fibers directions from the DTI analysis (as explained in the [Supporting Information](#) of Ref. 103). The fraction of WM fibers within the voxel, f_{WM} , can be estimated by counting the fraction of pixels in DTI images within the

spectroscopic voxel and that have high FA (e.g., ≥ 0.4); and $c_L \geq 0.4$, $c_P \leq 0.2$, and $c_S \leq 0.35$.¹¹⁶ c_L , c_P , and c_S are the coefficients of linearity, planarity, and sphericity, respectively. Note that this assumes maximal fiber anisotropy in WM (i.e., a worst-case scenario). The total signal attenuation for the modified randomly oriented infinite cylinders model then comprises two contributions: one coming from metabolites' diffusion in the GM (pure randomly oriented infinite cylinders), and the second coming from metabolites' diffusion in the WM modeled as diffusion within fibers distributed according to $P(\theta_i)$:

$$S(g, \delta, \Delta; D_{\text{intra}}, R) = (1 - f_{\text{WM}}) \frac{\int_0^\pi \sin(\theta) K(g, \theta, \delta, \Delta; D_{\text{intra}}, R) d\theta}{\int_0^\pi \sin(\theta) d\theta} + f_{\text{WM}} \frac{\sum_{i=1}^N P(\theta_i) K(g, \delta, \Delta; D_{\text{intra}}, R, \theta_i)}{\sum_{i=1}^N P(\theta_i)},$$

where the distribution $P(\theta_i)$ is the distribution of angles θ_i between the first eigenvector of the diffusion tensor and the diffusion-sensitizing gradients and is experimentally determined (hence the discrete summatory rather than a continuous integral). As already mentioned, if sensitivity to R is poor, then the signal attenuation K should be modeled as diffusion within sticks.

Conditions of applicability for diffusion time, b -value range and tissue composition are summarized in Table S2 for signal representations (monoexponential, kurtosis, and biexponential fits) and the randomly infinite oriented cylinders/sticks models.

5.2 | Considerations of noise and maximum b -value

The accuracy and precision of the ADC, apparent kurtosis (Kapp), and randomly oriented infinite cylinders model parameter estimates depend on σ , the SD of the Gaussian noise underpinning the dMRS signal decay normalized to the signal at $b=0 \text{ ms}/\mu\text{m}^2$. The σ can be estimated for measurements, for example, by computing the SD of the residuals from fitting the bi-exponential representation to normalized diffusion-weighted signals (Figure S1A) or from denoising techniques that also provide an estimate of the noise level.¹¹⁷

In Table 5, we show the simulated impact of noise on the relative bias and coefficient of variation of the different parameters. The ADC can be estimated accurately and precisely (i.e., both relative bias and coefficient of variation median and interquartile range $<10\%$) with $b_{\text{max}} < 5 \text{ ms}/\mu\text{m}^2$ and $\sigma \leq 0.04$. In contrast, Kapp can be

estimated accurately and precisely with $b_{\text{max}} < 10 \text{ ms}/\mu\text{m}^2$ only for low $\sigma \leq 0.01$. Regarding the randomly oriented infinite cylinders model with $b_{\text{max}} \leq 25 \text{ ms}/\mu\text{m}^2$, D_{intra} can be estimated accurately and precisely for $\sigma \leq 0.04$, whereas R can only be estimated accurately and precisely for very low $\sigma \ll 0.01$. If such a noise level cannot be achieved, we recommend using the randomly oriented sticks model.

The general recommendation is therefore to keep $\sigma \leq 0.04$; to accurately estimate ADC (with $b_{\text{max}} < 5 \text{ ms}/\mu\text{m}^2$) and D_{intra} (with $b_{\text{max}} \leq 25 \text{ ms}/\mu\text{m}^2$); $\sigma \leq 0.01$ when trying to estimate Kapp (with $b_{\text{max}} < 10 \text{ ms}/\mu\text{m}^2$); and $\sigma \ll 0.01$ when trying to estimate R (with $b_{\text{max}} \leq 25 \text{ ms}/\mu\text{m}^2$). Choices made from acquisitions to fitting (section 2–4) will impact σ and should therefore be carefully set up.

5.3 | Other models and representations

Beyond the monoexponential and kurtosis signal representations and the randomly oriented infinite cylinders/sticks biophysical models, we reference here other models and representations that can be of interest for the reader:

- Models and representations of dMRS diffusion time-dependence: Computational models of neuron-like digital substrates have been used to characterize the metabolites diffusion time-dependence and estimate from it microstructural features such as length and branching order of cellular processes.^{6,7,114,118}
- Models and representations of dMRS b -dependence at high b ($>10 \text{ ms}/\mu\text{m}^2$): The effect of secondary structures like dendritic spines and astrocytic leaflets has been investigated using signal representations and dMRS measurements at high b values and $10 < t_d < 100 \text{ ms}$ ^{119–121}; the overall complexity of cellular morphology has been investigated using signal representations derived from a fractional order formulation of the Bloch-Torrey equation.⁹⁸

6 | FUTURE DIRECTIONS

dMRS forms a lively research field that has taken off in the last 10 years. Although dMRS faces challenges regarding SNR, it has a great potential for probing, noninvasively, cell type-specific microstructure and could benefit directly from the latest developments in MRS and in dMRI. A few challenges awaiting solutions in acquisition, processing, fitting, and modeling are listed below. Solving these would unlock much of the potential of dMRS, both as a

TABLE 5 Simulated impact of Gaussian noise (for different standard deviation σ) on the relative bias and CV of ADC, Kapp, and randomly oriented infinite cylinders model parameters D_{intra} and R .

Representation or model	b_{max}	Parameter	$\sigma = 0.01$	$\sigma = 0.02$	$\sigma = 0.04$	$\sigma = 0.1$
Relative Bias: (Estimated–Ground Truth)/Ground Truth (%)						
Mono-exponential	5	ADC	-1 [-4; 1]	3 [-2; 7]	3 [-9; 14]	-9 [-27; 34]
	10	Not applicable	-	-	-	-
	25	Not applicable	-	-	-	-
Kurtosis	5	ADC	-2 [-7; 4]	-2 [-12; 6]	-4 [-19; 7]	6 [-27; 26]
		Kapp	3 [-78; 21]	-33 [-77; 22]	-32 [-87; 25]	-42 [-79; 12]
	10	ADC	-1 [-4; 3]	0 [-5; 8]	0 [-7; 10]	-1 [-16; 27]
		Kapp	-2 [-9; 1]	3 [-16; 16]	-25 [-38; 12]	-40 [-78; 15]
	25	Not applicable	-	-	-	-
				-	-	-
Randomly oriented infinite cylinders	5	D_{intra}	-7 [-22; -3]	-18 [-41; -4]	-31 [-45; -6]	-30 [-45; -10]
		R	22 [-39; 193]	113 [-17; 298]	143 [-36; 333]	178 [0; 391]
	10	D_{intra}	-3 [-8; 1]	-7 [-16; 1]	-15 [-35; -5]	-29 [-52; -6]
		R	2 [-61; 98]	44 [-34; 163]	87 [-27; 232]	217 [28; 486]
	25	D_{intra}	-1 [-4; 0]	-2 [-7; 3]	-5 [-15; 2]	-18 [-34; 1]
		R	1 [-40; 39]	-3 [-46; 72]	1 [-48; 136]	90 [-7; 241]
CV: std[Estimated]/mean[Estimated] (%)						
Mono-exponential	5	ADC	4 [2; 5]	5 [3; 7]	11 [8; 16]	26 [18; 38]
	10	Not applicable	-	-	-	-
	25	Not applicable	-	-	-	-
Kurtosis	5	ADC	4 [3; 6]	8 [5; 11]	13 [9; 19]	40 [23; 61]
		Kapp	39 [13; 149]	74 [32; 191]	99 [34; 290]	119 [51; 224]
	10	ADC	4 [3; 5]	7 [5; 9]	11 [9; 14]	21 [17; 31]
		Kapp	10 [6; 16]	14 [10; 34]	47 [23; 73]	97 [35; 185]
	25	Not applicable	-	-	-	-
				-	-	-
Randomly oriented infinite cylinders	5	D_{intra}	11 [6; 26]	26 [17; 35]	34 [25; 40]	47 [37; 58]
		R	99 [52; 156]	77 [41; 176]	99 [53; 242]	100 [44; 198]
	10	D_{intra}	5 [3; 7]	12 [8; 17]	21 [14; 33]	41 [31; 50]
		R	76 [42; 162]	88 [55; 170]	95 [71; 179]	72 [39; 166]
	25	D_{intra}	3 [2; 4]	6 [4; 7]	12 [8; 15]	35 [23; 42]
		R	49 [18; 121]	73 [39; 130]	85 [43; 166]	84 [58; 136]

Note: For each model parameter median [1st; 3rd] quartile values are reported. **Data simulation:** Analytical simulations were performed using the randomly oriented infinite cylinders model assuming an acquisition that can be run on both clinical and preclinical scanners: PGSE acquisition with $\theta/\gamma = 60/15$ ms; $b = 0, 1.5, 3, 5, 8.5, 15, 25$ ms/ μm^2 . The simulations were run for a range of realistic combinations of D_{intra} ($=0.2, 0.25, 0.30, 0.35, 0.40, 0.45, 0.50$ $\mu\text{m}^2/\text{ms}$) and R ($=0.25, 0.50, 0.75, 1.00, 1.25, 1.50, 2.00$ μm) values, with the addition of Gaussian noise corresponding to different σ levels. **Impact of Gaussian noise on parameter estimates:** To estimate the fit accuracy at different b_{max} , a Monte Carlo approach (250 draws; Figure S1B) was used to extract the median and the first and third quartiles of each parameter estimate. The fits were a mono-exponential decay for ADC, a kurtosis representation for ADC and Kapp, and a randomly oriented infinite cylinders model for D_{intra} and R . Note that at each new draw, new noisy signal is created by adding Gaussian noise with the SD estimated from the fitting residuals of the previous draw. Orange shadowed entries in the table highlight conditions where accuracy and precision was considered too low, that is, relative bias and CV median and interquartile range $>10\%$.

Abbreviations: CV, coefficient of variation; D_{intra} , intracellular diffusivity; PGSE, pulsed-gradient spin echo; R , radius.

research tool and for clinical use. These developments are interdependent and will benefit from each other:

- Faster scanning is crucial for clinical applications. A few approaches will make this possible:
 - Develop and validate simultaneous fitting approaches as proposed in Ref. 83 and integrated in FitAID⁷² and FSL-MRS,⁷³
 - Take advantage of the recent development of multiparametric acquisitions and use it to concurrently measure relaxation and diffusion for instance or better sample the q - t_d space,¹²²
 - Further develop and validate robust denoising approaches,¹¹⁷
 - Improve acquisitions methods (e.g., rapid diffusion tensor acquisition¹²³).
- Improve the spatial resolution and coverage with diffusion MRI.^{124,125}
- Develop cross-modalities approaches (e.g., dMRI and dMRS with a joint modeling of water and metabolites diffusion).
- Interpret the data with a metabolic or microstructural perspective (e.g., continuing the development of modeling to extract microstructural parameters, incorporation into simultaneous fitting, and accounting for metabolic complexity). Detailed authors contributions are specified in the Table S1

AFFILIATIONS

¹Wellcome Centre for Integrative Neuroimaging, FMRIB, Nuffield Department of Clinical Neurosciences, University of Oxford, Oxford, UK

²C.J. Gorter MRI Center, Department of Radiology, Leiden University Medical Center, Leiden, The Netherlands

³Cardiff University Brain Research Imaging Centre (CUBRIC), School of Psychology, Cardiff University, Cardiff, UK

⁴CIBM Center for Biomedical Imaging, Lausanne, Switzerland

⁵Departments of Biomedical Engineering and Radiology, University of Alberta, Alberta Edmonton, Canada

⁶Paris Brain Institute–ICM, Sorbonne University, UMR S 1127, Inserm U 1127, CNRS UMR 7225, Paris, France

⁷Animal Imaging and Technology, Ecole Polytechnique Fédérale de Lausanne, Lausanne, Switzerland

⁸Center for Magnetic Resonance Research, Department of Radiology, University of Minnesota, Minnesota, Minneapolis, USA

⁹Department of Radiology, Lausanne University Hospital, Lausanne, Switzerland

¹⁰Faculty of Biology and Medicine, University of Lausanne, Lausanne, Switzerland

¹¹Department of Diagnostic and Interventional Radiology, Technical University of Munich, Munich, Germany

¹²MR Methodology, Department for Diagnostic and Interventional Neuroradiology, University of Bern, Bern, Switzerland

¹³Translational Imaging Center (TIC), Swiss Institute for Translational and Entrepreneurial Medicine, Bern, Switzerland

¹⁴Danish Research Centre for Magnetic Resonance, Centre for Functional and Diagnostic Imaging and Research, Copenhagen University Hospital–Amager and Hvidovre, Hvidovre, Denmark

¹⁵Department of Health Technology, Technical University of Denmark, Lyngby, Denmark

¹⁶NMR Methods & Development Group, Max Planck Institute for Human Cognitive and Brain Sciences, Leipzig, Germany

¹⁷LIFMET, EPFL, Lausanne, Switzerland

¹⁸Université Paris-Saclay, CEA, CNRS, MIRCen, Laboratoires des Maladies Neurodégénératives, Fontenay-aux-Roses, France

¹⁹Department of Neurology, University of New Mexico School of Medicine, New Mexico Albuquerque, USA

²⁰Department of Physics and Astronomy, University of New Mexico School of Medicine, New Mexico Albuquerque, USA

²¹School of Computer Science and Informatics, Cardiff University, Cardiff, UK

²²Medical Radiation Physics, Clinical Sciences Lund, Lund University, Lund, Sweden

²³Department of Chemical and Biological Physics, The Weizmann Institute of Science, Rehovot, Israel

²⁴University Medical Center Utrecht, Utrecht, The Netherlands

²⁵Cardiff University Brain Research Imaging Centre (CUBRIC), School of Physics and Astronomy, Cardiff University, Cardiff, United Kingdom

²⁶Russell H. Morgan Department of Radiology and Radiological Science, The Johns Hopkins University School of Medicine, Maryland Baltimore, USA


²⁷F. M. Kirby Center for Functional Brain Imaging, Kennedy Krieger Institute, Maryland Baltimore, USA

²⁸Clinical Imaging Sciences Centre, Brighton and Sussex Medical School, Brighton, UK

ACKNOWLEDGMENTS

This paper was initiated by the workshop “Best Practices & Tools for Diffusion MR Spectroscopy,” held at the Lorentz Center (Leiden, Netherlands) in September 2021, and benefited from discussions among all (online and onsite) attendees (<https://www.lorentzcenter.nl/best-practices-en-tools-for-diffusion-mr-spectroscopy.html>). The workshop was also supported by NeurATRIS (A Translational Research Infrastructure for Biotherapies in Neurosciences, “Investissements d’Avenir”, ANR-11-INBS-0011).

ORCID

Clémence Ligneul  <https://orcid.org/0000-0001-5673-3009>

Chloé Najac  <https://orcid.org/0000-0002-7804-2281>

André Döring  <https://orcid.org/0000-0002-2096-5374>

Christian Beaulieu  <https://orcid.org/0000-0002-2342-3298>

Francesca Branzoli  <https://orcid.org/0000-0001-9792-0492>

William T. Clarke  <https://orcid.org/0000-0001-7159-7025>
 Cristina Cudalbu  <https://orcid.org/0000-0003-4582-2465>
 Guglielmo Genovese  <https://orcid.org/0000-0001-9409-0120>
 Saad Jbabdi  <https://orcid.org/0000-0003-3234-5639>
 Ileana Jelescu  <https://orcid.org/0000-0002-3664-0195>
 Dimitrios Karampinos  <https://orcid.org/0000-0003-4922-3662>
 Roland Kreis  <https://orcid.org/0000-0002-8618-6875>
 Henrik Lundell  <https://orcid.org/0000-0002-7044-442X>
 Małgorzata Marjańska  <https://orcid.org/0000-0002-4727-2447>
 Harald E. Möller  <https://orcid.org/0000-0002-5659-1925>
 Jessie Mosso  <https://orcid.org/0000-0001-6318-9507>
 Stefan Posse  <https://orcid.org/0000-0002-4816-080X>
 Stefan Ruschke  <https://orcid.org/0000-0001-9658-6541>
 Kadir Simsek  <https://orcid.org/0000-0003-4044-7395>
 Filip Szczepankiewicz  <https://orcid.org/0000-0002-5251-587X>
 Assaf Tal  <https://orcid.org/0000-0001-6718-6522>
 Chantal Tax  <https://orcid.org/0000-0002-7480-8817>
 Georg Oeltzschner  <https://orcid.org/0000-0003-3083-9811>
 Marco Palombo  <https://orcid.org/0000-0003-4892-7967>
 Itamar Ronen  <https://orcid.org/0000-0002-6872-4895>
 Julien Valette  <https://orcid.org/0000-0002-2067-5051>

TWITTER

Clémence Ligneul  [cleclouze](https://twitter.com/cleclouze)

REFERENCES

1. Yoo AJ, Gonzalez RG. Clinical applications of diffusion MR imaging for acute ischemic stroke. *Neuroimaging Clin N Am*. 2011;21:51-69.
2. Panagiotaki E, Chan RW, Dikaios N, et al. Microstructural characterization of normal and malignant human prostate tissue with vascular, extracellular, and restricted diffusion for cytometry in tumours magnetic resonance imaging. *Invest Radiol*. 2015;50:218-227.
3. Yoshizaki K, Seo Y, Nishikawa H, Morimoto T. Application of pulsed-gradient 31P NMR on frog muscle to measure the diffusion rates of phosphorus compounds in cells. *Biophys J*. 1982;38:209-211.
4. Moonen CT, van Zijl PC, Le Bihan D, DesPres D. In vivo NMR diffusion spectroscopy: 31P application to phosphorus metabolites in muscle. *Magn Reson Med*. 1990;13:467-477. doi:10.1002/mrm.1910130314
5. Choi JK, Dedeoglu A, Jenkins BG. Application of MRS to mouse models of neurodegenerative illness. *NMR Biomed*. 2007;20:216-237.
6. Palombo M, Ligneul C, Najac C, et al. New paradigm to assess brain cell morphology by diffusion-weighted MR spectroscopy in vivo. *Proc Natl Acad Sci U S A*. 2016;113:6671-6676.
7. Ligneul C, Palombo M, Hernandez-Garzon E, et al. Diffusion-weighted magnetic resonance spectroscopy enables cell-specific monitoring of astrocyte reactivity in vivo. *Neuroimage*. 2019;191:457-469.
8. Van Zijl PC, Moonen CT, Faustino P, Pekar J, Kaplan O, Cohen JS. Complete separation of intracellular and extracellular information in NMR spectra of perfused cells by diffusion-weighted spectroscopy. *Proc Natl Acad Sci U S A*. 1991;88:3228-3232.
9. Merboldt KD, Horstmann D, Hanicke W, Bruhn H, Frahm J. Molecular self-diffusion of intracellular metabolites in rat brain in vivo investigated by localized proton NMR diffusion spectroscopy. *Magn Reson Med*. 1993;29:125-129.
10. Wick M, Nagatomo Y, Prielmeier F, Frahm J. Alteration of intracellular metabolite diffusion in rat brain in vivo during ischemia and reperfusion. *Stroke*. 1995;26:1930-1933. discussion 1934.
11. Posse S, Cuenod CA, Le Bihan D. Human brain: proton diffusion MR spectroscopy. *Radiology*. 1993;188:719-725.
12. van Gelderen P, DesPres D, van Zijl PC, Moonen CT. Evaluation of restricted diffusion in cylinders. Phosphocreatine in rabbit leg muscle. *J Magn Reson B*. 1994;103:255-260.
13. Nicolay K, van der Toorn A, Dijkhuizen RM. In vivo diffusion spectroscopy. An overview. *NMR Biomed*. 1995;8:365-374.
14. Nicolay K, Braun KP, Graaf RA, Dijkhuizen RM, Kruiskamp MJ. Diffusion NMR spectroscopy. *NMR Biomed*. 2001;14:94-111.
15. Cohen Y, Assaf Y. High b-value q-space analyzed diffusion-weighted MRS and MRI in neuronal tissues—a technical review. *NMR Biomed*. 2002;15:516-542.
16. Ronen I, Valette J. Diffusion-weighted magnetic resonance spectroscopy. *EMagRes*. 2015;4:1471.
17. Palombo M, Shemesh N, Ronen I, Valette J. Insights into brain microstructure from in vivo DW-MRS. *Neuroimage*. 2018;182:97-116.
18. Cao P, Wu EX. In vivo diffusion MRS investigation of non-water molecules in biological tissues. *NMR Biomed*. 2017;30:e3481.
19. Dieckmeyer M, Ruschke S, Eggers H, et al. ADC quantification of the vertebral bone marrow water component: removing the confounding effect of residual fat. *Magn Reson Med*. 2017;78:1432-1441.
20. Wu M, Junker D, Branca RT, Karampinos DC. Magnetic resonance imaging techniques for brown adipose tissue detection. *Front Endocrinol (Lausanne)*. 2020;11:421.
21. Lehnert A, Machann J, Helms G, Claussen CD, Schick F. Diffusion characteristics of large molecules assessed by proton MRS on a whole-body MR system. *Magn Reson Imaging*. 2004;22:39-46.
22. Cao P, Fan SJ, Wang AM, et al. Diffusion magnetic resonance monitors intramyocellular lipid droplet size in vivo. *Magn Reson Med*. 2015;73:59-69.
23. Verma SK, Nagashima K, Yaligar J, et al. Differentiating brown and white adipose tissues by high-resolution diffusion NMR spectroscopy. *J Lipid Res*. 2017;58:289-298.

24. Weidlich D, Honecker J, Gmach O, et al. Measuring large lipid droplet sizes by probing restricted lipid diffusion effects with diffusion-weighted MRS at 3T. *Magn Reson Med*. 2019;81:3427-3439.
25. Weidlich D, Zamskiy M, Maeder M, Ruschke S, Marburg S, Karampinos DC. Reduction of vibration-induced signal loss by matching mechanical vibrational states: application in high b-value diffusion-weighted MRS. *Magn Reson Med*. 2020;84:39-51.
26. Brandejsky V, Boesch C, Kreis R. Proton diffusion tensor spectroscopy of metabolites in human muscle in vivo. *Magn Reson Med*. 2015;73:481-487.
27. Brandejsky V, Kreis R, Boesch C. Restricted or severely hindered diffusion of intramyocellular lipids in human skeletal muscle shown by in vivo proton MR spectroscopy. *Magn Reson Med*. 2012;67:310-316.
28. Ruschke S, Kienberger H, Baum T, et al. Diffusion-weighted stimulated echo acquisition mode (DW-STEAM) MR spectroscopy to measure fat unsaturation in regions with low proton-density fat fraction. *Magn Reson Med*. 2016;75:32-41.
29. Wang AM, Cao P, Yee A, Chan D, Wu EX. Detection of extracellular matrix degradation in intervertebral disc degeneration by diffusion magnetic resonance spectroscopy. *Magn Reson Med*. 2015;73:1703-1712.
30. Wang AM, Leung GK, Kiang KM, Chan D, Cao P, Wu EX. Separation and quantification of lactate and lipid at 1.3 ppm by diffusion-weighted magnetic resonance spectroscopy. *Magn Reson Med*. 2017;77:480-489.
31. de Graaf RA, Brown PB, McIntyre S, Nixon TW, Behar KL, Rothman DL. High magnetic field water and metabolite proton T1 and T2 relaxation in rat brain in vivo. *Magn Reson Med*. 2006;56:386-394.
32. Haase A, Frahm J, Matthaei D, Hanicke W, Merboldt KD. FLASH imaging: rapid NMR imaging using low flip-angle pulses. 1986. *J Magn Reson*. 2011;213:533-541.
33. Kan HE, Techawiboonwong A, van Osch MJ, et al. Differences in apparent diffusion coefficients of brain metabolites between grey and white matter in the human brain measured at 7 T. *Magn Reson Med*. 2012;67:1203-1209.
34. Genovese G, Marjanska M, Auerbach EJ, et al. In vivo diffusion-weighted MRS using semi-LASER in the human brain at 3 T: methodological aspects and clinical feasibility. *NMR Biomed*. 2021;34:e4206.
35. Ligneul C, Palombo M, Valette J. Metabolite diffusion up to very high b in the mouse brain in vivo: revisiting the potential correlation between relaxation and diffusion properties. *Magn Reson Med*. 2017;77:1390-1398.
36. Stejskal O, Tanner JE. Spin diffusion measurements: spin echoes in the presence of a time-dependent field gradient. *J Chem Phys*. 1965;42:288-292.
37. Neeman M, Freyer JP, Sillerud LO. A simple method for obtaining cross-term-free images for diffusion anisotropy studies in NMR microimaging. *Magn Reson Med*. 1991;21:138-143.
38. Jara H, Wehrli FW. Determination of background gradients with diffusion MR imaging. *J Magn Reson Imaging*. 1994;4:787-797.
39. Szczepankiewicz F, Sjolund J. Cross-term-compensated gradient waveform design for tensor-valued diffusion MRI. *J Magn Reson*. 2021;328:106991.
40. Scheenen TW, Klomp DW, Wijnen JP, Heerschap A. Short echo time 1H-MRSI of the human brain at 3T with minimal chemical shift displacement errors using adiabatic refocusing pulses. *Magn Reson Med*. 2008;59:1-6.
41. Garwood M, DelaBarre L. The return of the frequency sweep: designing adiabatic pulses for contemporary NMR. *J Magn Reson*. 2001;153:155-177.
42. Shemesh N, Rosenberg JT, Dumez JN, Muniz JA, Grant SC, Frydman L. Metabolic properties in stroked rats revealed by relaxation-enhanced magnetic resonance spectroscopy at ultrahigh fields. *Nat Commun*. 2014;5:4958.
43. Mougel E, Malaquin S, Vincent M, Valette J. Using spectrally-selective radiofrequency pulses to enhance lactate signal for diffusion-weighted MRS measurements in vivo. *J Magn Reson*. 2022;334:107113.
44. Mosso J, Simicic D, Lanz B, Gruetter R, Cudalbu C. Diffusion-weighted SPECIAL improves the detection of J-coupled metabolites at ultra-high magnetic field. *Magn Reson Med*. 2023. doi:10.1002/mrm.29805
45. Mlynárik V, Gambarota G, Frenkel H, Gruetter R. Localized short-echo-time proton MR spectroscopy with full signal-intensity acquisition. *Magnetic Resonance in Medicine*. 2006;56(5):965-970. <https://doi.org/10.1002/mrm.21043>
46. Dreher W, Leibfritz D. New method for the simultaneous detection of metabolites and water in localized in vivo 1H nuclear magnetic resonance spectroscopy. *Magn Reson Med*. 2005;54:190-195.
47. Giapitzakis IA, Shao T, Avdievich N, Mekle R, Kreis R, Henning A. Metabolite-cycled STEAM and semi-LASER localization for MR spectroscopy of the human brain at 9.4T. *Magn Reson Med*. 2018;79:1841-1850.
48. Doring A, Adalid V, Boesch C, Kreis R. Diffusion-weighted magnetic resonance spectroscopy boosted by simultaneously acquired water reference signals. *Magn Reson Med*. 2018;80:2326-2338.
49. Doring A, Kreis R. Magnetic resonance spectroscopy extended by oscillating diffusion gradients: cell-specific anomalous diffusion as a probe for tissue microstructure in human brain. *Neuroimage*. 2019;202:116075.
50. Hajnal JV, Bryant DJ, Kasuboski L, et al. Use of fluid attenuated inversion recovery (FLAIR) pulse sequences in MRI of the brain. *J Comput Assist Tomogr*. 1992;16:841-844.
51. Wilson M, Andronesi O, Barker PB, et al. Methodological consensus on clinical proton MRS of the brain: review and recommendations. *Magn Reson Med*. 2019;82:527-550.
52. Oz G, Deelchand DK, Wijnen JP, et al. Advanced single voxel (1) H magnetic resonance spectroscopy techniques in humans: experts' consensus recommendations. *NMR Biomed*. 2020;34:e4236.
53. Andronesi OC, Bhattacharyya PK, Bogner W, et al. Motion correction methods for MRS: experts' consensus recommendations. *NMR Biomed*. 2021;34:e4364.
54. Schirmer T, Auer DP. On the reliability of quantitative clinical magnetic resonance spectroscopy of the human brain. *NMR Biomed*. 2000;13:28-36.

55. Palacios EM, Martin AJ, Boss MA, TRACK-TBI Investigators. Toward precision and reproducibility of diffusion tensor imaging: a multicenter diffusion phantom and traveling volunteer study. *AJNR Am J Neuroradiol*. 2017;38:537-545.
56. Valette J, Guillermier M, Besret L, et al. Isoflurane strongly affects the diffusion of intracellular metabolites, as shown by ¹H nuclear magnetic resonance spectroscopy of the monkey brain. *J Cereb Blood Flow Metab*. 2007;27:588-596.
57. Provencher SW. Estimation of metabolite concentrations from localized in vivo proton NMR spectra. *Magn Reson Med*. 1993;30:672-679.
58. Wood ET, Ercan E, Sati P, Cortese ICM, Ronen I, Reich DS. Longitudinal MR spectroscopy of neurodegeneration in multiple sclerosis with diffusion of the intra-axonal constituent N-acetylaspartate. *Neuroimage Clin*. 2017;15:780-788.
59. Deelchand DK, Auerbach EJ, Marjanska M. Apparent diffusion coefficients of the five major metabolites measured in the human brain in vivo at 3T. *Magn Reson Med*. 2018;79:2896-2901.
60. Moonen CT, Van Zijl PCM. Highly effective water suppression for in vivo proton NMR spectroscopy (DRYSTEAM). *J Magn Reson (1969)*. 1990;88:28-41.
61. Cudalbu C, Behar KL, Bhattacharyya PK, et al. Contribution of macromolecules to brain (¹H) MR spectra: experts' consensus recommendations. *NMR Biomed*. 2021;34:e4393.
62. Knight-Scott J. Application of multiple inversion recovery for suppression of macromolecule resonances in short echo time (¹H) NMR spectroscopy of human brain. *J Magn Reson*. 1999;140:228-234.
63. Kunz N, Cudalbu C, Mlynarik V, Huppi PS, Sizonenko SV, Gruetter R. Diffusion-weighted spectroscopy: a novel approach to determine macromolecule resonances in short-echo time ¹H-MRS. *Magn Reson Med*. 2010;64:939-946.
64. Ligneul C, Valette J. Probing metabolite diffusion at ultra-short time scales in the mouse brain using optimized oscillating gradients and "short"-echo-time diffusion-weighted MRS. *NMR Biomed*. 2017;30:e3671.
65. Klose U. In vivo proton spectroscopy in presence of eddy currents. *Magn Reson Med*. 1990;14:26-30.
66. Kreis R, Boer V, Choi IY, et al. Terminology and concepts for the characterization of in vivo MR spectroscopy methods and MR spectra: background and experts' consensus recommendations. *NMR Biomed*. 2020;34:e4347.
67. Lin C, Wendt RE 3rd, Evans HJ, Rowe RM, Hedrick TD, LeBlanc AD. Eddy current correction in volume-localized MR spectroscopy. *J Magn Reson Imaging*. 1994;4:823-827.
68. Near J, Harris AD, Juchem C, et al. Preprocessing, analysis and quantification in single-voxel magnetic resonance spectroscopy: experts' consensus recommendations. *NMR Biomed*. 2021;34:e4257.
69. Wilson M. Adaptive baseline fitting for ¹H MR spectroscopy analysis. *Magn Reson Med*. 2021;85:13-29.
70. Poullet JB, Sima DM, Simonetti AW, et al. An automated quantitation of short echo time MRS spectra in an open source software environment: AQSES. *NMR Biomed*. 2007;20:493-504.
71. Simpson R, Devenyi GA, Jezzard P, Hennessy TJ, Near J. Advanced processing and simulation of MRS data using the FID appliance (FID-A)-an open source, MATLAB-based toolkit. *Magn Reson Med*. 2017;77:23-33.
72. Chong DG, Kreis R, Bolliger CS, Boesch C, Slotboom J. Two-dimensional linear-combination model fitting of magnetic resonance spectra to define the macromolecule baseline using FiTAID, a fitting tool for arrays of interrelated datasets. *MAGMA*. 2011;24:147-164.
73. Clarke WT, Stagg CJ, Jbabdi S. FSL-MRS: an end-to-end spectroscopy analysis package. *Magn Reson Med*. 2021;85:2950-2964.
74. Stefan D, Di Cesare F, Andrasescu A, et al. Quantitation of magnetic resonance spectroscopy signals: the jMRUI software package. *Meas Sci Technol*. 2009;20:104035.
75. Oeltzschner G, Zollner HJ, Hui SCN, et al. Osprey: open-source processing, reconstruction & estimation of magnetic resonance spectroscopy data. *J Neurosci Methods*. 2020;343:108827.
76. Borbath T, Murali-Manohar S, Dorst J, Wright AM, Henning A. ProFit-1D-A 1D fitting software and open-source validation data sets. *Magn Reson Med*. 2021;86:2910-2929.
77. Wilson M. spant: an R package for magnetic resonance spectroscopy analysis. *J Open Source Softw*. 2021;6:3646.
78. Wilson M, Reynolds G, Kauppinen RA, Arvanitis TN, Peet AC. A constrained least-squares approach to the automated quantitation of in vivo (¹H) magnetic resonance spectroscopy data. *Magn Reson Med*. 2011;65:1-12.
79. Soher BJ, Semanchuk P, Todd D, Steinberg J, Young K. VeSPA: integrated applications for RF pulse design, spectral simulation and MRS data analysis. In Proceedings of the 19th Annual Meeting of ISMRM, Montréal, Québec, Canada 2011 p. 1410.
80. Clayton DB, Elliott MA, Leigh JS, Lenkinski RE. ¹H spectroscopy without solvent suppression: characterization of signal modulations at short echo times. *J Magn Reson*. 2001;153:203-209.
81. Simsek K, Doring A, Pampel A, Moller HE, Kreis R. Macromolecular background signal and non-Gaussian metabolite diffusion determined in human brain using ultra-high diffusion weighting. *Magn Reson Med*. 2022;88:1962-1977.
82. Simicic D, Rackayova V, Xin L, et al. In vivo macromolecule signals in rat brain (¹H)-MR spectra at 9.4T: parametrization, spline baseline estimation, and T(2) relaxation times. *Magn Reson Med*. 2021;86:2384-2401.
83. Adalid V, Doring A, Kyathanahally SP, Bolliger CS, Boesch C, Kreis R. Fitting interrelated datasets: metabolite diffusion and general lineshapes. *MAGMA*. 2017;30:429-448.
84. Landheer K, Gajdosik M, Juchem C. A semi-LASER, single-voxel spectroscopic sequence with a minimal echo time of 20.1 ms in the human brain at 3 T. *NMR Biomed*. 2020;33:e4324.
85. Novikov DS, Kiselev VG, Jespersen SN. On modeling. *Magn Reson Med*. 2018;79:3172-3193.
86. Valette J, Ligneul C, Marchadour C, Najac C, Palombo M. Brain metabolite diffusion from ultra-short to ultra-long time scales: what do we learn, where should we go? *Front Neurosci*. 2018;12:2.
87. Ellegood J, Hanstock CC, Beaulieu C. Considerations for measuring the fractional anisotropy of metabolites with diffusion tensor spectroscopy. *NMR Biomed*. 2011;24:270-280.

88. Landheer K, Juchem C. Are Cramer-Rao lower bounds an accurate estimate for standard deviations in in vivo magnetic resonance spectroscopy? *NMR Biomed.* 2021;34:e4521.
89. Zollner HJ, Povazan M, Hui SCN, Tapper S, Edden RAE, Oeltzschner G. Comparison of different linear-combination modeling algorithms for short-TE proton spectra. *NMR Biomed.* 2021;34:e4482.
90. Giapitzakis IA, Borbath T, Murali-Manohar S, Avdievich N, Henning A. Investigation of the influence of macromolecules and spline baseline in the fitting model of human brain spectra at 9.4T. *Magn Reson Med.* 2019;81:746-758.
91. Soher BJ, Young K, Maudsley AA. Representation of strong baseline contributions in 1H MR spectra. *Magn Reson Med.* 2001;45:966-972.
92. Najac C, Doring A, Clarke W, et al. Differences in diffusion-weighted MRS processing and fitting pipelines, and their effect on tissue modeling: results from a workshop challenge. Proceedings of the Joint Annual Meeting ISMRM-ESMRMB & ISMRT 31st Annual Meeting, London, UK 2022 p. 2616.
93. Tal A. The future is 2D: spectral-temporal fitting of dynamic MRS data provides exponential gains in precision over conventional approaches. *Magn Reson Med.* 2023; 89:499-507.
94. Clarke WT, Ligneul C, Cottaar M, Ip IB, Jbabdi S. Universal dynamic fitting of magnetic resonance spectroscopy. *bioRxiv.* 2023. doi:10.1101/2023.06.15.544935
95. Marjanska M, Deelchand DK, Kreis R, 2016 ISMRM MRS Study Group Fitting Challenge Team. Results and interpretation of a fitting challenge for MR spectroscopy set up by the MRS study group of ISMRM. *Magn Reson Med.* 2022; 87:11-32.
96. Marjanska M, Terpstra M. Influence of fitting approaches in LCModel on MRS quantification focusing on age-specific macromolecules and the spline baseline. *NMR Biomed.* 2021;34:e4197.
97. Assaf Y, Cohen Y. Structural information in neuronal tissue as revealed by q-space diffusion NMR spectroscopy of metabolites in bovine optic nerve. *NMR Biomed.* 1999;12:335-344.
98. Ingo C, Brink W, Ercan E, Webb AG, Ronen I. Studying neurons and glia non-invasively via anomalous subdiffusion of intracellular metabolites. *Brain Struct Funct.* 2018;223:3841-3854.
99. Assaf Y, Cohen Y. Non-mono-exponential attenuation of water and N-acetyl aspartate signals due to diffusion in brain tissue. *J Magn Reson.* 1998;131:69-85.
100. Branzoli F, Ercan E, Webb A, Ronen I. The interaction between apparent diffusion coefficients and transverse relaxation rates of human brain metabolites and water studied by diffusion-weighted spectroscopy at 7 T. *NMR Biomed.* 2014;27:495-506.
101. Mougél E, Malaquin S, Valette J. Assessing potential correlation between T(2) relaxation and diffusion of lactate in the mouse brain. *Magn Reson Med.* 2022; 88:2277-2284.
102. Kroenke CD, Ackerman JJ, Yablonskiy DA. On the nature of the NAA diffusion attenuated MR signal in the central nervous system. *Magn Reson Med.* 2004;52:1052-1059.
103. Palombo M, Ligneul C, Valette J. Modeling diffusion of intracellular metabolites in the mouse brain up to very high diffusion-weighting: diffusion in long fibers (almost) accounts for non-monoexponential attenuation. *Magn Reson Med.* 2017;77:343-350.
104. Ronen I, Budde M, Ercan E, Annese J, Techawiboonwong A, Webb A. Microstructural organization of axons in the human corpus callosum quantified by diffusion-weighted magnetic resonance spectroscopy of N-acetylaspartate and post-mortem histology. *Brain Struct Funct.* 2014;219:1773-1785.
105. Lundell H, Ingo C, Dyrby TB, Ronen I. Cytosolic diffusivity and microscopic anisotropy of N-acetyl aspartate in human white matter with diffusion-weighted MRS at 7 T. *NMR Biomed.* 2021;34:e4304.
106. Najac C, Marchadour C, Guillemier M, et al. Intracellular metabolites in the primate brain are primarily localized in long fibers rather than in cell bodies, as shown by diffusion-weighted magnetic resonance spectroscopy. *Neuroimage.* 2014;90:374-380.
107. Shemesh N, Jespersen SN, Alexander DC, et al. Conventions and nomenclature for double diffusion encoding NMR and MRI. *Magn Reson Med.* 2016;75:82-87.
108. Henriques RN, Palombo M, Jespersen SN, Shemesh N, Lundell H, Ianus A. Double diffusion encoding and applications for biomedical imaging. *J Neurosci Methods.* 2021;348:108989.
109. Shemesh N, Rosenberg JT, Dumez JN, Grant SC, Frydman L. Distinguishing neuronal from astrocytic subcellular microstructures using in vivo double diffusion encoded 1H MRS at 21.1 T. *PLoS One.* 2017;12:e0185232.
110. Vincent M, Palombo M, Valette J. Revisiting double diffusion encoding MRS in the mouse brain at 11.7T: which microstructural features are we sensitive to? *Neuroimage.* 2020;207:116399.
111. Lundell H, Najac C, Bulk M, Kan HE, Webb AG, Ronen I. Compartmental diffusion and microstructural properties of human brain gray and white matter studied with double diffusion encoding magnetic resonance spectroscopy of metabolites and water. *Neuroimage.* 2021;234:117981.
112. Linse P, Söderman O. The validity of the short-gradient-pulse approximation in NMR studies of restricted diffusion. Simulations of molecules diffusing between planes, in cylinders and spheres. *J Magn Reson A.* 1995;116:77-86.
113. Szczepankiewicz F, Sjolund J, Stahlberg F, Latt J, Nilsson M. Tensor-valued diffusion encoding for diffusional variance decomposition (DIVIDE): technical feasibility in clinical MRI systems. *PLoS One.* 2019;14:e0214238.
114. Ianus A, Alexander DC, Zhang H, Palombo M. Mapping complex cell morphology in the grey matter with double diffusion encoding MR: a simulation study. *Neuroimage.* 2021;241:118424.
115. Palombo M, Alexander DC, Zhang H. Large-scale analysis of brain cell morphometry informs microstructure modelling of gray matter. In Proceedings of the 2021 ISMRM & SMRT Annual Meeting and Exhibition, Virtual Meeting 2021.
116. Fieremans E, Jensen JH, Helpert JA. White matter characterization with diffusional kurtosis imaging. *Neuroimage.* 2011;58:177-188.
117. Mosso J, Simicic D, Simsek K, Kreis R, Cudalbu C, Jelescu IO. MP-PCA denoising for diffusion MRS data: promises and pitfalls. *Neuroimage.* 2022;263:119634.

118. Van Nguyen D, Grebenkov D, Le Bihan D, Li JR. Numerical study of a cylinder model of the diffusion MRI signal for neuronal dendrite trees. *J Magn Reson*. 2015;252:103-113.
119. Palombo M, Ligneul C, Hernandez-Garzon E, Valette J. Can we detect the effect of spines and leaflets on the diffusion of brain intracellular metabolites? *Neuroimage*. 2017;182:283-293.
120. Yablonskiy DA, Sukstanskii AL. Theoretical models of the diffusion weighted MR signal. *NMR Biomed*. 2010;23:661-681.
121. Palombo M, Gallea C, Genovese G, Lehericy S, Branzoli F. Characterizing the fine microstructure of cerebellar and cerebral cortex non-invasively with metabolite diffusion-weighted MRS. In Proceedings of the 28th Annual Meeting of ISMRM & SMRT, Virtual Conference 2020.
122. Kulpanovich A, Tal A. What is the optimal schedule for multiparametric MRS? A magnetic resonance fingerprinting perspective. *NMR Biomed*. 2021;34:e4196.
123. Hanstock C, Beaulieu C. Rapid acquisition diffusion MR spectroscopy of metabolites in human brain. *NMR Biomed*. 2021;34:e4270.
124. Ercan AE, Techawiboonwong A, Versluis MJ, Webb AG, Ronen I. Diffusion-weighted chemical shift imaging of human brain metabolites at 7T. *Magn Reson Med*. 2015;73:2053-2061.
125. Fotso K, Dager SR, Landow A, et al. Diffusion tensor spectroscopic imaging of the human brain in children and adults. *Magn Reson Med*. 2017;78:1246-1256.

SUPPORTING INFORMATION

Additional supporting information may be found in the online version of the article at the publisher's website.

FIGURE S1. Schematic to clarify the difference between (A) the level of noise σ of the normalized dMRS signal decay and (B) how Monte-Carlo simulations help estimating the model accuracy.

TABLE S1. Detail of author contributions (* equally contributed).

TABLE S2. Conditions of applicability for diffusion time, b-value range and tissue composition for signal representations (monoexponential, kurtosis, and biexponential fits) and the randomly oriented infinite cylinders/sticks models.

How to cite this article: Ligneul C, Najac C, Döring A, et al. Diffusion-weighted MR spectroscopy: Consensus, recommendations, and resources from acquisition to modeling. *Magn Reson Med*. 2023;1-26. doi: 10.1002/mrm.29877